JGR Solid Earth

RESEARCH ARTICLE
10.1029/2023JB027126

Special Section:
Understanding and anticipating Induced Seismicity: from mechanics to seismology

Impacts of Rate of Change in Effective Stress and Inertial Effects on Fault Slip Behavior: New Insights Into Injection-Induced Earthquakes

Zihan Sun[1,2], Derek Elsworth[3], Guanglei Cui[1,2], Yingchun Li[4], Aiyu Zhu[5], and Tianyu Chen[1,2]

[1]Key Laboratory of Ministry of Education on Safe Mining of Deep Metal Mines, School of Resources and Civil Engineering, Northeastern University, Shenyang, China, [2]Key Laboratory of Liaoning Province on Deep Engineering and Intelligent Technology, Northeastern University, Shenyang, China, [3]Department of Energy and Mineral Engineering, G3 Center and Energy Institute, The Pennsylvania State University, University Park, PA, USA, [4]State Key Laboratory of Coastal and Offshore Engineering, Dalian University of Technology, Dalian, China, [5]Institue of Geophysics, China Earthquake Administration, Beijing, China

Abstract Understanding the physical mechanisms which link fluid injection with triggered earthquakes is critical in minimizing hazard in subsurface fluid-injection operations. Currently, injection-induced changes in effective stress on faults are considered as the main criterion in triggering seismic fault slip. However, rate of change in effective stress, together with inertial effects, are also be implicated in this criterion. We present a modified critical stiffness criterion to investigate the relative likelihood of triggering earthquakes during injection for different injection rate schedules (constant-vs-cycled-vs-increasing). A stability analysis of fault stress is used to define a critical stiffness as a function of magnitudes and rate of change in effective stresses. The relative potential for triggering earthquakes due to fluid injection is investigated using a coupled fluid-flow-deformation model. Polarities of change in critical stiffness are employed as an index to define the tendency for a transition from aseismic to seismic reactivation. During constant rate injection and self-equilibration stages, the absolute magnitude of effective stress controls the transition. Conversely, the rate of change in effective stress dominates this transition when injection suddenly starts or stops, and inertial effects suppress the transformation to seismic slip. Cycling injection rates into a given fault is the most stable, followed by constant injection, with linear injection the least stable for the same total volume injected. High permeability reservoirs and strike-slip faulting regimes reduce the potential of inducing seismicity. This work provides both new insights into assessing the seismic risks associated with injection and guidance for mitigation.

Plain Language Summary During subsurface operations, fluid injections can lower fault strength and trigger slip on pre-existing faults. This slip may be aseismic (no earthquake) or seismic (earthquake), being controlled by the fault critical stiffness - determined from fault frictional characteristics and stress state. The stiffness change can be quantified in terms of the absolute fault stress magnitude and its rate of change, induced by the fluid injection. This change may be used to determine the tendency of reactivation as either aseismic or seismic. From our analysis, the rate of change in effective stress dominates the likelihood of triggering earthquakes as injection rates suddenly change. Suddenly stopping injection readily triggers earthquakes and inertial effects helpfully restrain the transition from aseismic and seismic slip-on faults. Cycled injection and high permeability reservoirs are the most effective factors in minimizing seismicity. This study provides a new insight to understand and mitigate earthquake occurrence during subsurface fluid injection.

Key Points:

- The rate of change in effective stress on a fault determines the likelihood of triggering seismicity when injection suddenly starts or stops
- Inertial effects restrain the transition between aseismic and seismic reactivation over the injection period
- Stress transfer can increase effective stress during constant injection and drive seismic slip

Supporting Information:

Supporting Information may be found in the online version of this article.

Correspondence to:

G. Cui,
cuiguanglei@mail.neu.edu.cn

Citation:

Sun, Z., Elsworth, D., Cui, G., Li, Y., Zhu, A., & Chen, T. (2024). Impacts of rate of change in effective stress and inertial effects on fault slip behavior: New insights into injection-induced earthquakes. *Journal of Geophysical Research: Solid Earth*, *129*, e2023JB027126. https://doi.org/10.1029/2023JB027126

Received 24 MAY 2023
Accepted 24 JAN 2024

Author Contributions:

Conceptualization: Zihan Sun, Derek Elsworth, Guanglei Cui, Yingchun Li, Aiyu Zhu, Tianyu Chen
Data curation: Zihan Sun, Derek Elsworth, Guanglei Cui, Yingchun Li
Formal analysis: Zihan Sun, Derek Elsworth, Guanglei Cui, Yingchun Li
Funding acquisition: Tianyu Chen
Investigation: Zihan Sun
Methodology: Zihan Sun, Derek Elsworth, Guanglei Cui, Yingchun Li, Aiyu Zhu
Software: Zihan Sun, Guanglei Cui

1. Introduction

In addition to a majority of natural earthquakes, the remaining seismic events are related to anthropogenic activities (Yehya, et al., 2022), viz, water injection induced earthquakes (Alghannam & Juanes, 2020; Healy et al., 1968). The injection of large volumes of fluids into the Earth's subsurface has the potential to elevate fluid pressures and reactivate faults (Cappa et al., 2009; Keranen et al., 2014; Luccio et al., 2018; Zoback & Gorelick, 2012). Consequently, subsurface fluid injection is treated as one of the prominent factors contributing to induced earthquakes (Foulger et al., 2018). Fluid-injection-induced earthquakes impede the rapid development of geo-energy systems, such as CO_2 geological storage (Pacala & Socolow, 2004; Vidal-Gilbert et al., 2010), and hydraulic stimulation in Enhanced Geothermal Systems. Experimental and theoretical studies have explored the

Supervision: Derek Elsworth, Guanglei Cui, Yingchun Li, Aiyu Zhu, Tianyu Chen
Validation: Zihan Sun
Visualization: Zihan Sun
Writing – original draft: Zihan Sun
Writing – review & editing: Zihan Sun, Derek Elsworth, Guanglei Cui, Yingchun Li, Aiyu Zhu

link between injecting large volumes of fluid into the subsurface and triggering seismicity (Chiodini et al., 2020; Spagnuolo et al., 2016; Verdon, 2014). However, a complete understanding of the potential of triggering large seismic events as a result of injection is underdeveloped, for instance, the impacts of the magnitude and the rate of change in effective stress on the resulting timing and likelihood of such triggered seismic events.

Massive fluid injection leads to a reduction in effective stress on embedded faults ($\sigma_n - p$) (Ruina, 1983; Scuderi & Collettini, 2016; Terzaghi, 1923) (where σ_n and p represent the norml stress and pore pressure, respectively) and a concomitant decrease in frictional strength under constant normal stress (Figure 1). These processes can result in fault reactivation - either aseismic or seismic. Therefore, characterizing the occurrence and likelihood of various modes of fault frictional slip is essential in addressing injection-triggered earthquakes (Alghannam & Juanes, 2020; Goodfellow et al., 2015; Guglielmi et al., 2015). Frictional sliding can occur as creep or stick-slip behavior, which can be captured in stick-slip experiments (Brace & Byerlee, 1966), when the injection-induced slip is either aseismic or seismic (Das & Zoback, 2011; Goodfellow et al., 2015; Guglielmi et al., 2015; Warpinski et al., 2012). Frictional behavior on faults is commonly modeled by Rate-and-state friction (RSF), which accommodates the major impacts of frictional properties on slip behavior and defines step changes in the friction coefficient during the full seismic cycle (Dieterich, 1972; James, 1978). Combining RSF with a simple spring-slider model (Rice & Ruina, 1983; Ruina, 1983; Tullis & Weeks, 1986) yields a criterion, referred to as the critical stiffness of the fault, to modulate the transition from stable to unstable sliding (Rice, 1993; Ruina, 1983) and determine whether the modes of fault frictional slip can trigger earthquakes (Leeman et al., 2016; Scuderi & Collettini, 2016). In previous studies, the classical definition of critical stiffness is represented as $k_{crit} = (\sigma_n - p)\ (b - a)/d_c$, where $(b - a)$, d_c are the constitutive parameters and characteristic sliding distance, respectively—recovered from frictional experiments (Gu et al., 1984; Leeman et al., 2016; Rice, 1993). With this relationship, fault stability is linked to both effective-stress- and velocity-weakening rate-state parameters (Rice & Ruina, 1983; Ruina, 1983). When the loading system stiffness, represented as k_s (Leeman et al., 2016; Scuderi & Collettini, 2016), is lower than the value of critical stiffness ($k_s < k_{\mathrm{crit}}$), the fault slips seismically (Rice, 1993) and vice versa. Specifically, when $(b - a) < 0$ (i.e., $k_{\mathrm{crit}} < 0$), then $k_s > k_{\mathrm{crit}}$ is always satisfied and the fault slips stably until new induced factors emerge (Kang et al., 2019; Zhu & Kang, 2020). Therefore, a positive value of the parameter $(b - a)$ is mandatory for seismic slip.

The concept of critical stiffness can be applied to estimate the anticipated likelihood of induced earthquakes, caused by fault slip, and to scale this possibility with changing pore pressure (Ruina, 1983). However, a growing number of field observations suggest that fluid-injection rate can indeed impact the occurrence of induced earthquakes (Guglielmi et al., 2015; Segall & Lu, 2015; Weingarten et al., 2015). For example, (a) stress measurements at injection sites indicate that very small increases in fluid pressure are capable of triggering slip on faults (Chiaramonte et al., 2008); moreover, (b) deep borehole stress measurements at the Mountaineer coal-burning power plant indicate a severe limitation in the injection rate, above which CO_2 injection will result in unstable slip (Lucier et al., 2006). An increase in injection rate generally correlates with an increased frequency of induced earthquakes (Healy et al., 1968; Improta et al., 2015; Langenbruch & Zoback, 2016), and abrupt increases or decreases in injection rates tend to immediately precede the occurrence of such earthquakes (Kim, 2013; Tang et al., 2018). Therefore, the likelihood of triggering an earthquake also depends on the rate of pressurization rather than merely on the pressure magnitude (Alghannam & Juanes, 2020). To characterize this effect of the injection rate on the likelihood of seismicity, we present a modified critical stiffness in a spring-slider model that can represent such poroelastic processes.

Dynamic effects must also be considered in defining the critical stiffness of the fault since inertial effects intrinsically resist motion (Cueto-Felgueroso et al., 2018) and the shear strength of the fault is related to the current slip state. In the classical approach, the inertial effect ($-\rho \frac{\partial^2 u}{\partial t^2}$, representing the tendency of a geological body in motion to stay in motion, where ρ represents the density and u denotes the displacement) is defined by the elasto-dynamic response which is both complex and compute-intensive to obtain (Rice, 1993). As an alternative, quasi-static equilibrium can be adopted with a slip-velocity-dependent radiation-daming approximation ($-\xi \frac{\partial u}{\partial t}$, denoting the elastodynamic inertial effect, where ξ indicates the viscous damping factor (Rice, 1993)). The approximation is employed to describe the dependence of shear strength on the current slip state of the fault (Pampillón et al., 2018). Over the last decade, the radiation-damping term has been widely applied to approximate inertial effects in injection-induced earthquake sequences on faults (Cueto-Felgueroso et al., 2018; Pampillón et al., 2018; Rice, 1993). In previous work (Cueto-Felgueroso et al., 2018;

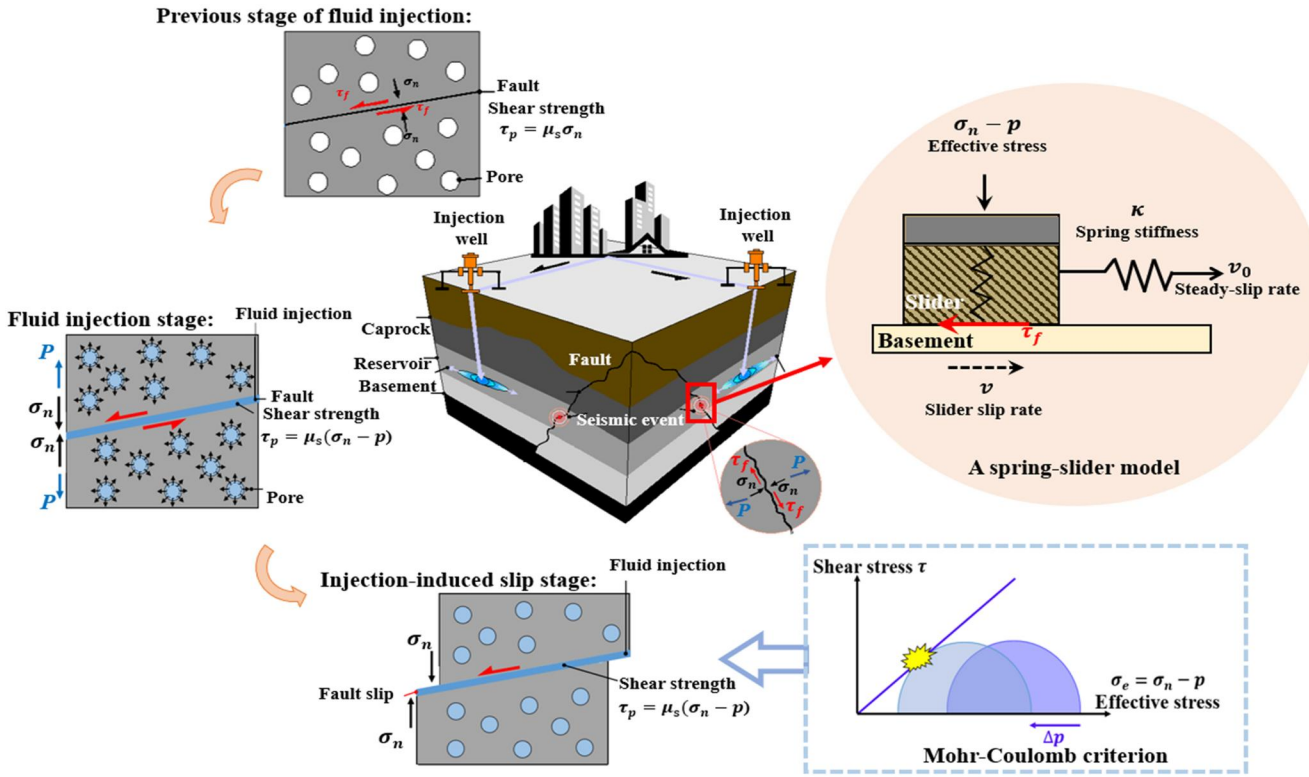

Figure 1. Schematic illustration of the physical mechanisms that can trigger fault reactivation during injection, where τ_p is the peak shear strength, τ_f is the dynamic shear strength, μ_s is the static friction coefficient, σ_n is the normal stress, p is the pore pressure, K is the spring stiffness of slider, and v_0 is the steady-slip rate.

Pampillón et al., 2018), the impact of inertial effects on injection-induced earthquakes has been characterized and transient fluctuations of pore pressure and solid stresses during rupture have been considered. These studies suggest that radiation damping is used to characterize the impact of inertial effects on injection-induced seismicity, and they additionally address the issue where the neglect of radiation damping allows unbounded slip velocities and hence overestimates actual earthquake magnitudes (Cueto-Felgueroso et al., 2018; Pampillón et al., 2018).

In the following, we use the concept of fault critical stiffness to both evaluate fault instability and to explain the elusive dependencies of triggering earthquakes on the magnitude and change rate of pore pressure. This appropriately accommodates instantaneous changes in normal stress that result from un/partially drained fluid injection that have previously been ignored. Furthermore, the impact of inertial effects, which are characterized by radiation damping, are also considered in our definition of critical stiffness. These allow an improved prediction of the likelihood of injection-induced earthquakes as a result of rates of fluid injection. This new approach and related results are reported in the following.

2. Mathematical Model

We consider a reservoir, fault and the surrounding rock as a poroelastic medium (Biot, 1941) where the elastic skeleton is isotropic, homogeneous and saturated by a single slightly compressible fluid. In the following subsections we describe the constitutive model for the deformability of the porous medium, conservation of mass for the fluid, the Mohr-Coulomb failure criterion, importantly culminating in a modified representation of critical stiffness. These governing equations describe the transient response of a homogeneous poroelastic domain by assuming that (a) the mechanical and transport properties of the rock remain unchanged, (b) deformation remains infinitesimal and elastic, and (c) temperature effects are ignored (Pampillón et al., 2018).

2.1. Coupled Simulation for Fault/Reservoir

2.1.1. Reservoir and Fault Deformation

For a homogeneous, isotropic and elastic medium, considering the influence of pore pressure, the Navier-type constitutive law, which governs the deformation of both the reservoir and the fault, is expressed as (Detournay & Cheng, 1993; Liu et al., 2010):

$$G_m u_{i,kk} + \frac{G_m}{1-2\nu} u_{k,ki} = f_i + \alpha_m p_m \tag{1}$$

where u is the displacement, the α_m denotes the Biot coefficient, p_m is the fluid pressure, and G_m is the shear modulus, with the subscript m representing the form of the medium as either a fault or a reservoir. The subscripts i and k represent the directional components of the variables, the subscript kk is the Einstein summation convention, and a subscripted comma represents the time derivative of a variable. The terms on the right represent the body force per unit volume, resulting from fluid injection.

2.1.2. Governing Equation of Fluid Flow

Considering the effect of gravity, fluid mass conservation in the reservoir and fault can be expressed as (Biot, 1941; Darcy, 1856):

$$\rho_m S \frac{\partial(p_m)}{\partial t} + \rho_m \alpha_m \frac{\partial(\varepsilon_v)}{\partial t} = \nabla \cdot \left(\rho_m \frac{k_m}{\mu_v} (\nabla p_m - g) \right) \tag{2}$$

$$S = \varnothing_m \chi_f + (1 - \varnothing_m) \chi_p \tag{3}$$

where ρ_m is the fluid density, S is the storage coefficient, and $\varnothing_m$ is the porosity. χ_f, χ_p are compressibility of fluid and effective compressibility of matrix as 4.0×10^{-10} (1/Pa) and 1.0×10^{-4} (1/Pa), respectively. ε_v is the volumetric strain, k_m is the permeability of both the reservoir and fault, μ_v is the dynamic viscosity, and g is the gravitational acceleration.

2.2. Mohr-Coulomb Criterion

For the uniformly pressurized fault, the Mohr-Coulomb criterion, combined with the effective stress law (Terzaghi, 1923), defines the potential for reactivation with injection. The effective stress, peak frictional strength and shear stress on the fault change during fluid injection. Failure occurs when the peak shear strength (τ_p) is exceeded by the shear stress (τ) of the fault (Jaeger et al., 2009) as

$$\tau \geq \tau_p = \mu_s \sigma_e = \mu_s (\sigma_n - p) \tag{4}$$

where μ_s is the static friction coefficient, with σ_e, $\sigma_e = \sigma_n - p$ as the effective stress and σ_n as the normal stress that acts on the fault. Here, we assume that compression is positive, and that tension is negative. The normal and shear stress components act on a fault with normal direction and stress vector defined in the Cauchy stress form (Atanackovic & Guran, 2000).

2.3. Modified Critical Stiffness Criterion

2.3.1. Frictional Strength Evolution

The dynamic frictional strength of the fault, τ_f, is defined by an adapted Mohr-Coulomb criterion (Pampillón et al., 2018) as:

$$\tau_f = \mu(v,\theta)\sigma_e + \xi v + \tau_c \tag{5}$$

where τ_c is the cohesive strength (hereafter, $\tau_c = 0$) and $\mu(v,\theta)$ is the dynamic friction coefficient which is slip-velocity- and state-dependent.

We employ the radiation-damping approximation (a velocity-dependent term, ξv), instead of the direct elastodynamic inertial effect, to represent the inertial effects of the porous medium, where $\xi = \zeta G/2c_s$ with G as the shear modulus and c_s as the shear-wave speed, defined as $c_s = \sqrt{G/\rho_d}$ and ρ_d as the dry-rock density. In this contribution, we introduce the term, ξv, since: (a) the response of continuum models to an abrupt change in stress τ along the rupture plane leads into an instantaneous change in the slip velocity rather than the acceleration; (b) the value of ξ can exactly incorporate the elastodynamic effect of the instantaneous changes in the time histories of the shear stress and slip velocity; (c) the parameter ζ denotes a dimensionless parameter and its value is related to the recurrence interval between earthquakes. A large magnitude of ζ denotes a shorter recurrence time and a lower stress drop, thus leading to a small fault slip (Rice, 1993). In this study, an extra coefficient ζ with a value of 10^6 is added to the radiation damping coefficient to represent a recurrence period of 35 years (Rice, 1993).

2.3.2. Spring-Slider Model

A single-degree-of-freedom spring-slider model is employed to model the effects of effective stress on a slipping fault core (Alghannam & Juanes, 2020; Cueto-Felgueroso et al., 2018; Rice, 1993). As shown in Figure 1, the model consists of a slider of unit base area, pulled by a spring, the end of which is constrained to move at a steady slip rate. The slider represents the fault core and the vertical spring inside the slider is analogous to the poroelastic rock skeleton sandwiching the fault (compressed due to the transmission of pressures). The slip state of the slider represents the fluid injection-driven reactivation process of the fault. A piston is loaded vertically which compresses the vertical spring and acts as the effective stress applied on the fault. The spring-slider system consists of a spring, representing the fault stiffness, and a slider, denoting the frictional response of the fault core. An elastic compliance is incorporated in the spring of stiffness k_s (Rice, 1993) estimated from the shear modulus of the surrounding fault and from the characteristic length of the slipping fault (Ruina, 1983). The horizontal stress acting on the slider is specified as the difference between the shear stress on the fault and the frictional resistance between the fault-damage zone and the fault core. The poroelastic shear stress of the slider is represented by the tensile stress in the spring and characterized by the length of the spring. In the initial state, both the slider and spring are constrained to move at a steady slip rate v_0 with no relative displacement. After fluid injection or liquid drainage, the length of the spring is changed, with the constant applied velocity v_0 of the load point and that of the slider v slipping with different velocities. Therefore, a relative displacement builds between the load point and the slider, U. $U = 0$ only if $v_0 = v$. In this study, our model accounts for the poroelastic coupling between the shear stresses and effective normal stresses along the fault.

Momentum balance for the spring-slider idealization results in (Byerlee, 1970; Iverson, 2005; Rice & Tse, 1986; Segall & Rice, 1995)

$$(\sigma_n - p)\mu(v,\theta) + \xi v - k_s U = 0 \tag{6}$$

$$\dot{U} = v_0 - v \tag{7}$$

where U is the displacement from v_0 to v, k_s is the stiffness of the loading system (spring-slider), and ξv is the radiation damping. The superscripted dot represents the time derivative.

Ruina's slip law is adopted for the friction coefficient (Ruina, 1983):

$$\mu(v,\theta) = \mu^* + a\, ln\frac{v}{v^*} + \theta \tag{8}$$

where a is the "direct-effect" derived from friction experiments, v^* is a normalizing velocity, μ^* is a constant that is appropriate for steady state at velocity v^* and θ is the state variable.

Linker and Dieterich (1992) proposed a rate-state evolution model, considering the effective stress principle then:

$$\dot{\theta} = -\frac{v}{d_c}\left(\theta + b\, ln\frac{v}{v^*}\right) - \alpha\frac{\dot{\sigma_e}}{\sigma_e} \tag{9}$$

where d_c is the characteristic sliding distance, b is a constitutive parameter and α is a scaling factor, respectively defined via experimental measurements.

2.3.3. Linear Stability Analysis

A linear stability analysis may be applied to define the mode of fault slip—aseismic or seismic (Ruina, 1983; Segel & Slemrod, 1989). In this method, the dynamic process is considered as a series of quasi-steady-state processes. The constitutive model is linearly expanded and then a stability analysis is conducted to obtain the stability condition of the system for a small perturbation. This process is similar to the linear stability analysis employed by Ruina to recover the steady-state stability condition for a constant pore pressure (Ruina, 1983; Segel & Slemrod, 1989). However, in this case, not only the pore pressure but also the effective stress varies with time and depends on the poroelastic and hydraulic parameters of the fault and reservoir. Thus, this linear stability analysis is used to recover the stability condition under the condition of constant effective stress. Similar to previous work (Ruina, 1983; Segel & Slemrod, 1989), effective stress is first held constant to obtain a quasi-steady state and then a linear stability analysis is performed on the poroelastic spring–slider system at a fixed effective stress. Equations 8 and 9 are first linearized about the quasi-steady state and then substituted into Equation 6, to define

$$\sigma_e\theta^* + \frac{\alpha\sigma_e v^*}{v_0} + \xi v^* = k_s U^* \tag{10}$$

Taking the time derivative of Equation 8 yields

$$\dot{v}^* = \frac{v_0}{\xi v_0 + a(\sigma_n - p)}\left[-\frac{\alpha(\dot{\sigma_n} - \dot{p})}{v_0} + \frac{b(\sigma_n - p)}{d_c} - k_s + \frac{\xi(\dot{\sigma_n} - \dot{p})}{(\sigma_n - p)}\right]v^* + \frac{v_0}{\xi v_0 + a(\sigma_n - p)}\left[\frac{v_0(\sigma_n - p)}{d_c}\right]\theta^* \tag{11a}$$

$$\dot{\theta}^* = \left(\frac{\alpha(\dot{\sigma_n} - \dot{p})}{v_0(\sigma_n - p)} - \frac{b}{d_c}\right)v^* - \frac{v_0}{d_c}\theta^* \tag{11b}$$

These equations represent a 2×2 autonomous system of linear ordinary differential equations with solutions of the form $\tau^* = ReA_1e^{\lambda t}$ and $\theta^* = ReA_2e^{\lambda t}$, where Re is the real component of the operator, both A_1 and A_2 are constants, λ is the growth rate and t is time. Substituting these forms into Equation 11 results in the characteristic equation:

$$\lambda^2 + \left[\frac{v_0}{d_c} - \frac{v_0}{\xi v_0 + a(\sigma_n - p)}\left(-\frac{\alpha(\dot{\sigma_n} - \dot{p})}{v_0} + \frac{b(\sigma_n - p)}{d_c} - \kappa_s + \frac{\xi(\dot{\sigma_n} - \dot{p})}{(\sigma_n - p)}\right)\right]\lambda - \frac{v_0}{\xi v_0 + a(\sigma_n - p)}\left[\frac{k_s v_0}{d_c} - \frac{\xi v_0(\dot{\sigma_n} - \dot{p})}{d_c(\sigma_n - p)}\right] = 0 \tag{12}$$

If the real part of the roots λ_i are negative for all i, then perturbations of the slider are damped, and the spring-slider system is stable. In other words, the stress disturbance due to fluid injection can be self-dissipated and the fault is stable. Conversely, if the real part of the roots λ_i is positive for some i, then perturbations of the slider grow exponentially, and the spring-slider system is unstable. While in this situation, the stress disturbance is uncontrolled and divergent, leading to the unstable state of the fault.

According to the discriminant of the roots to this equation, we obtain the modified critical stiffness:

$$k_{crit} = -\frac{\alpha(\dot{\sigma_n} - \dot{p})}{v_0} + \frac{(b - a)(\sigma_n - p)}{d_c} + \xi\left[\frac{(\dot{\sigma_n} - \dot{p})}{(\sigma_n - p)} - \frac{v_0}{d_c}\right] \tag{13}$$

Accordingly, frictional instability for the spring-slider system with evolving effective stress depends not only on the magnitude ($\frac{(b-a)(\sigma_n-p)}{d_c}$) and change rate of the effective stress ($-\frac{\alpha(\dot{\sigma_n}-\dot{p})}{v_0}$), but also on the change in the radiation damping ($\xi\left[\frac{(\dot{\sigma_n}-\dot{p})}{(\sigma_n-p)} - \frac{v_0}{d_c}\right]$). Therefore, if the stiffness of the loading system is lower than a critical value (Equation 13), the system becomes unstable, and stick-slip can be triggered as seismic fault slip; otherwise, this system

remains stable and returns aseismic slip. We use this more complete definition of critical stiffness in the following to determine the likelihood of fault slip transitioning from stability-to-instability or vice versa as a result of fluid injection. (Details for derivation in Text S1 in Supporting Information S1)

3. Numerical Model

CO_2 storage in suitable geological repositories, as a critical issue in environmental protection, is one viable strategy for reducing emissions and minimizing economic disruption when de-carbonizing energy supply (Pacala & Socolow, 2004; Vidal-Gilbert et al., 2010). Thus, we consider CO_2 geological sequestration as a type-example to explore the potential for injection-induced earthquakes. A modified critical stiffness criterion incorporates magnitudes and rate of change in effective stress as well as radiation damping and is used as a proxy in defining the likelihood for a transition to seismic fault slip during CO_2 injection. We use a distributed parameter poro-mechanical model, implemented into and solved through COMSOL Multiphysics (Version 5.4), to define stress changes for an idealized reservoir-fault geometry to define the evolution of critical stiffness.

3.1. Model Geometry and Mesh

We represent a reservoir-fault system as a rectangular block ($26 \times 16 \times 5.65$ km), which is further subdivided into subunits as shown in Figure 2a. A 150 m thick layer at 1.5 km depth represents a CO_2 storage reservoir. A 60° east-dipping structure of a ~10.1 m width fault transects the reservoir and subdivides it into three sections. Furthermore, the fault is divided into a 10-cm-wide fault core and a 10-m-wide fault damage zone flanking the core (Rice, 2006). Above and below the reservoir are the surrounding cap- and floor-rocks. An injection well is represented by a vertical line that transects the reservoir, 1.50 km from the fault core and is located at center in the x-direction. The specific location for the calculation (monitoring area) within the simulation model is in the fault core at the junction between the fault and the reservoir with the same x-coordinate of the fluid injection well (as shown in Figure 2a).

The geologic structure of the fault is first meshed because of its small thickness at the scale of only several meters. A mesh distribution is enforced on the fault edge to ensure that at least three elements represent the width of the fault core and 10 elements the damage zone (in the y-direction) with 32 elements in the x-direction and 90 elements in the z-direction (as shown in Figure 2b). With these settings, the elements are meshed throughout the full fault domain. The remaining parts of the geological body are meshed to conform to this with a denser mesh generated toward the fault to achieve a smooth transition from meter (fault) to kilometer (reservoir) scales. The left block of the model is meshed with the sweep feature using hexahedral elements. For the right block a fine mesh of tetrahedral elements is adopted. With these settings, there are 31,680 hexahedral elements in the fault and 23,556 tetrahedral and 4,800 hexahedral elements in the reservoir with an element quality of 0.77 and 0.80 for fault and reservoir, respectively.

3.2. Parameters and Boundary Conditions

This simulation model was established as a conceptual model to explore the physical mechanisms that link CO_2 injection with the triggering of earthquakes—defined by the evolution of critical stiffness of the fault over the full duration of CO_2 injection. The case of a depleted (hydrocarbon) reservoir was selected as a representative geological host characterized by a relatively large reservoir permeability (1.0×10^{-15} m^2) and small initial pore pressure (2.0×10^6 Pa) (James, 2014). The fault core generally consists of low-permeability gouge that are either cataclasites or ultracataclasites (or a combination of the two) (Caine et al., 1996; Knipe, 1992; Vrolijk et al., 2016). The higher-permeability damage zone generally consists of fractures over a wide range of length scales and subsidiary faults. In other words, the low-permeability fault core acts as a barrier to prevent fluid from penetrating across fault, while the fault damage zone provides relatively more permeable channels for transmitting fluids parallel to the fault. Here, we set the permeability values of $1.0 \times 10^{-15}/1.0 \times 10^{-18}$ m^2 (Yehya et al., 2018) for the fault damage zone and fault core. The parameters governing the slip behavior are set as $\mu_s = 0.5$, $\alpha = 0.4$, $b-a = 1.0 \times 10^{-4}$ (Marone, 1998), with a characteristic slip distance as $d_c = 1 \times 10^{-2}$ m and reference velocity as $v_0 = 1 \times 10^{-6}$ m/s (Aharonov & Scholz, 2017; Ito & Ikari, 2016). The related parameters are listed in Table 1.

The Solid Mechanics module in COMSOL was adopted in order to implement the reservoir-/fault-deformation process. In the benchmark model, the stress regime of the geological system is that of a normal fault ($\sigma_v \geq \sigma_x \geq \sigma_y$),

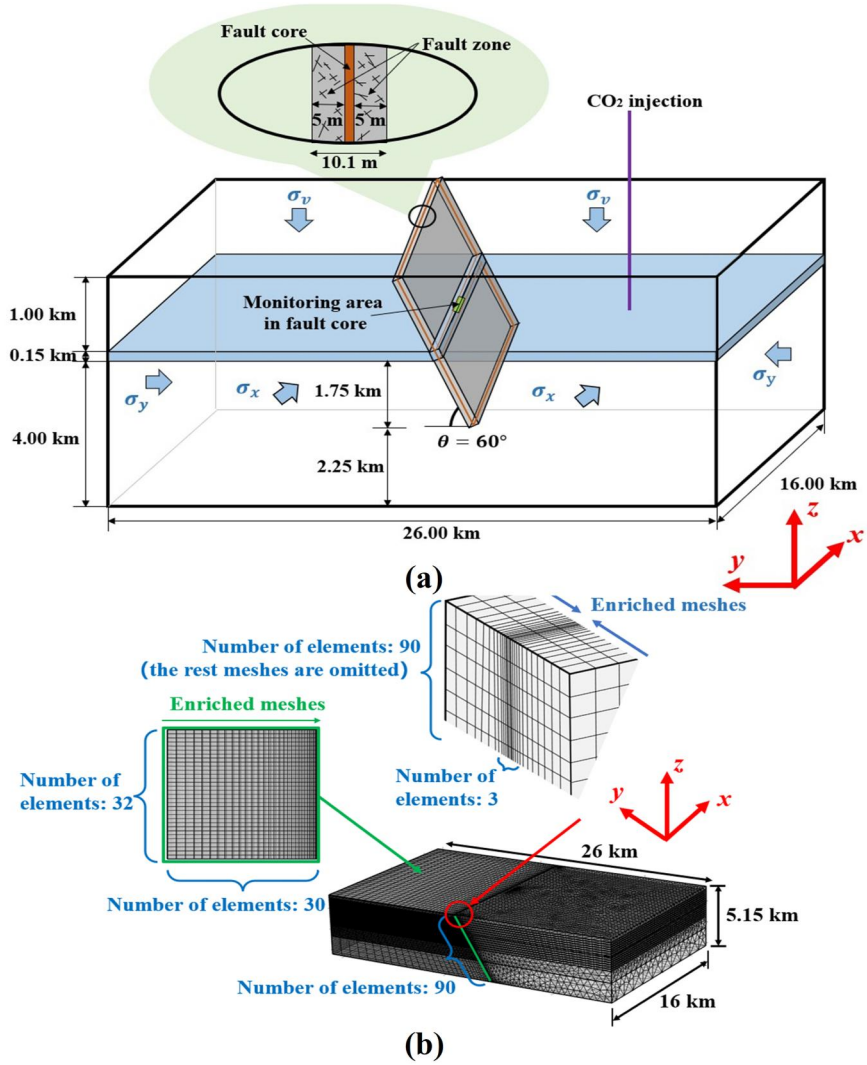

Figure 2. 3D schematic and meshing schematic of the numerical model, where σ_v is the vertical stress, σ_x represents the horizontal stress in the x-direction, σ_y denotes the horizontal stress in the y-direction and θ is the dip angle of the fault from the horizontal. (a). 3D schematic of a numerical model that represents CO_2 injection into a confined reservoir that is transected by a fault. (b). Meshing schematic of the numerical model.

with σ_v denoting vertical stress, the σ_x acting in the x-direction and σ_y acting in the y-direction. To achieve these stress constraints, the initial stress is specified, and the stress gradient defined as 25.0 MPa/km in the z-direction with the value of 20.0 MPa/km in the x-direction and 16.5 MPa/km the y-direction. The reservoir is 1,000 m deep and therefore features stresses of 25.0, 20.0 and 16.5 MPa in the z-, x- and y-directions forming a 3D stress state. The model base was fixed to zero displacement in all directions with the top surface free to displace.

Darcy's law is applied in the porous medium and the Subsurface Flow module in COMSOL is employed. CO_2 was injected into the reservoir through a vertical injection well at a constant injection rate using wellbore boundary conditions via mass flow. The surrounding far-field boundaries were represented as no-flow boundaries. CO_2 injection was continuous and at a constant rate, followed by a shut-off period in order to characterize the impacts of fluid migration in the fault and reservoir. The equations of fluid flow and solid mechanics are fully coupled within the "time-dependent" solution. To this end, a single large system of equations, which include all of the couplings simultaneously, are solved within a single iteration in COMSOL Multiphysics.

Table 1
Model Parameters

Symbol	Parameter	Value	Unit
E	Young's modulus	2.0×10^{10}	Pa
υ	Poisson's ratio	0.25	–
k_m	Initial reservoir permeability	1.0×10^{-15}	– m^2
k_f	Initial fault zone/core permeability	$1.0 \times 10^{-15}/1.0 \times 10^{-18}$	m^2
P_0	Initial pore pressure	2.0×10^{6}	Pa
ϕ_m	Porosity	0.10	–
σ_v	Vertical stress	2.5×10^{7}	Pa
σ_x	x- direction- horizontal stress	2.0×10^{7}	Pa
σ_y	y-direction horizontal stress	1.7×10^{7}	Pa
ξ	Damping viscous factor	2.0×10^{12}	Pa/(m/s)
$b - a$	Velocity-weakening parameters	1.0×10^{-4}	–
A	Normalized frictional parameter	0.40	–
d_c	Characteristic slip distance	1.0×10^{-2}	m
v_0	Initial slip velocity	1.0×10^{-6}	m/s
μ_s	Static friction coefficient	0.5	–

4. Model Results

The Mohr-Coulomb failure criterion (Equation 4) was employed to determine whether a fault is reactivated, and the likelihood of injection-induced earthquakes depends on the magnitude of the critical stiffness. Equation 13 infers that the critical stiffness of the fault is inversely correlated with rate of change in effective stress and is positively related to the magnitude of effective stress under conditions of evolving normal stress. Moreover, inertial effects also exert a significant impact on the seismic response (Pampillón et al., 2018). In the present work, we thus first confirm whether a fault can slip with changes in the Coulomb stresses, and then specifically consider two significant factors—those are, both the change in effective stress acting on the fault and inertial effects—as well as their net effect on critical stiffness of fault and potentially inducing earthquakes. In the following subsections, the critical stiffness of the monitored area, located at the junction between the fault and the reservoir (Figure 2a), is evaluated for illustration.

4.1. Fluid Injection Induced Fault Reactivation and the Likelihood of Seismic Slip

4.1.1. Stress Changes and Fault Reactivation

As a result of injection (Figure 3), the variation of effective stress in the fault core (at the junction position between the fault and reservoir) and its resolved stresses (pore pressure and normal stress) are evaluated over four stages, as illustrated in Figure 4a. (a) In the first stage, the CO_2 diffuses into reservoir and arrives at the fault as shown in Figure 3a. The pore pressure in the fault damage zone increases and exerts an added confinement on the low-permeability fault core (Fan et al., 2019)—defined as the "confinement effect" in this work. The normal stress on the fault core increases rapidly and the change in effective stress on fault core is equivalent to that of increasing normal stress because the variation in pore pressure in the low-permeability fault core remains negligible compared with that of normal stress. Therefore, the fluid injection rapidly increases effective stress as shown in the first stage of Figure 4a. (b) The CO_2 further diffuses along the fault damage zone (Figure 3b) and continues enhancing the extrusion effect exerted on the monitoring area but with a smaller rate of increase (second stage of Figure 4a). Thus, the normal stress and the effective stress still increase, but at a reduced rate compared with the first stage; (c) After shut-in, injection suddenly stops, while fluid permeates further into the fault and reservoir (Figure 3c), and the pore pressure in the reservoir and fault-damage zone decreases together with the normal stress applied in the fault core. The effective stress in the fault core declines sharply, as shown in the third stage of Figure 4a. (d) In the fourth stage, the fault-reservoir system equilibrates (Figure 3d). In this stage, the pore

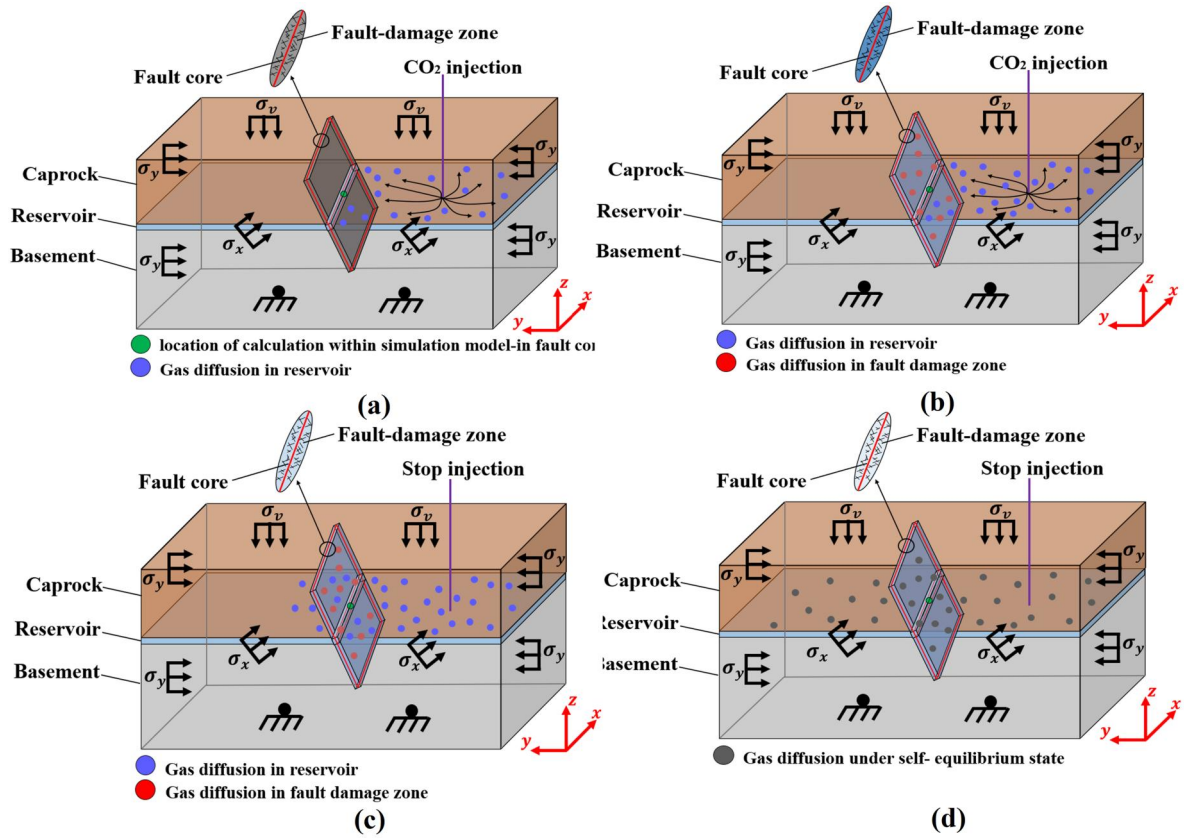

Figure 3. Schematic illustration of pressure diffusion in the reservoir and fault during CO_2 injection. (a). The first stage (injection suddenly starts): CO_2 diffusion within the reservoir alone. (b). The second stage (constant injection stage): CO_2 migration into the fault-damage zone. (c). The third stage (injection suddenly stops): CO_2 continues to diffuse in the reservoir and fault. (d). The fourth stage (self-equilibrium stage): Steady-state distribution of CO_2 in the reservoir and fault. In all subplots, the green symbol denotes the monitoring location in the fault core, the blue symbols represent gas/pressure diffusion in the reservoir, the red symbols represent gas/pressure in the fault-damage zone, and the gray symbols represent the gas/pressure diffusion in the equilibrium state.

pressures in the reservoir and fault damage zone further reduce toward the long term near-equilibrium. Correspondingly, the normal stress and effective stress in the fault core decrease—approaching a steady value as shown in the fourth stage of Figure 4a. In the entire CO_2 injection process, the pore pressure in the fault core varies over only a small range for the low permeability of fault core (Anyim & Gan, 2020; Gan & Lei, 2020).

The fault is reactivated once the shear stress on the fault reaches frictional strength, which varies with changing effective stress, as based on the Mohr-Coulomb criterion. As illustrated in Figure 4b, the shear stress on the fault core decreases in the first stage and rapidly increases in the constant injection stage (the second stage). Then the shear stress on the fault core exceeds the peak value of frictional strength in the third stage and rapidly deceases in the self-equilibration stage (the fourth stage). As shown in Figure 4b, the difference between shear stress and peak value of frictional strength of the fault core is positive in the second and third stages, which indicates that the fault slips. Therefore, it is necessary to evaluate the seismic risk of the slipping fault when injection continues but then suddenly stops.

4.1.2. Impact of Effective Stress on Critical Stiffness

The evolution of the impact of the magnitude and rate of change of effective stress on the critical stiffness of the fault in the above mentioned four stages is illustrated in Figure 5a. (a) In the first stage, the pressure front arrives at the fault-damage zone and compresses the fault core (poroelastic confinement effect), thereby rapidly increasing the normal stress and resulting in an increased rate of change in effective stress (Figure 4a). The increment of normal stress is fully transferred to the enhanced effective stress due to the minimal change in pore pressure within the fault core. The increased effective stress enhances the critical stiffness of the fault, and the increasing rate of effective stress decreases the critical stiffness (Equation 13). The competition between effective stress

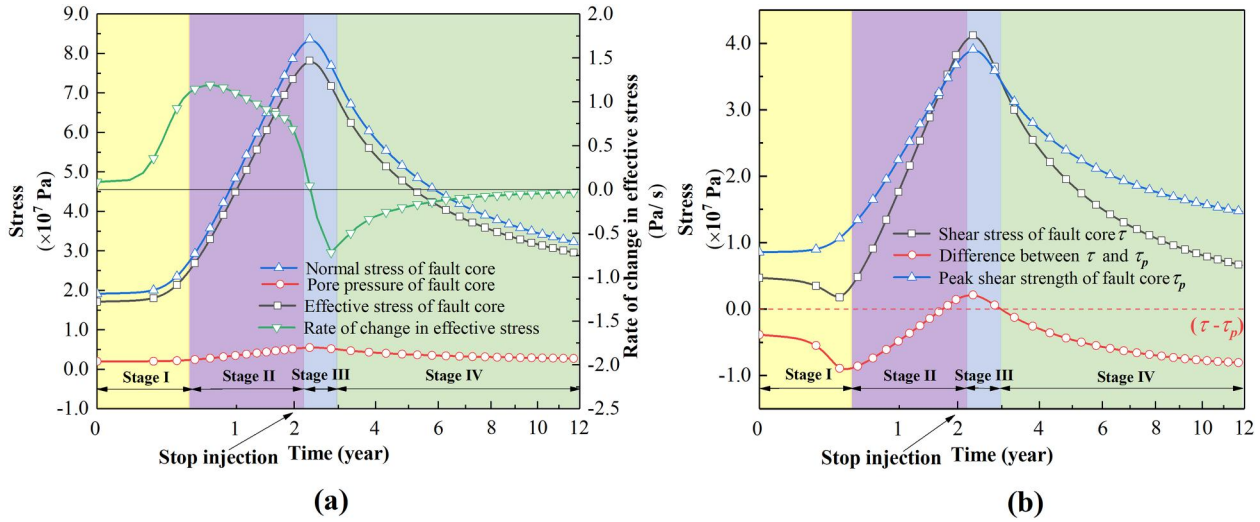

Figure 4. Coulomb stress changes in the fault core during CO_2 injection. (a). Variation of effective stress of fault core and its resolved stress. (b). Evolution of shear stress and peak shear strength in the fault core and the difference between them.

magnitude and its rate of change overall decreases the critical stiffness and potentially drives an aseismic response of the fault. (b) In the second stage, the effective stress in the fault core, generated by the confinement effect, increases slower than in the first stage, which leads to a decrease in the rate of effective stress change but remains positive overall (Figure 4). Therefore, both the enhanced effective stress and its decreasing rate increase the critical stiffness and tend to enhance the likelihood for seismic slip. (c) In the third stage, the CO_2 diffuses further into the reservoir and the confinement effect reduces when injection stops. Both the normal stress and effective stress of the fault decrease represented as a negative rate of change. The decreasing effective stress reduces the critical stiffness and conversely the decreasing rate of change in effective stress increases the critical stiffness. The competition between the effective stress magnitude and its rate of change enhances the critical stiffness and increases the likelihood of seismic slip. (d) In the fourth stage, the effective stress decreases at a slower rate compared with that in the third stage and evolves to a steady value with a decreasing rate that approaches zero. Both the reduced effective stress and its rate decrease the critical stiffness and result in an aseismic response of the fault.

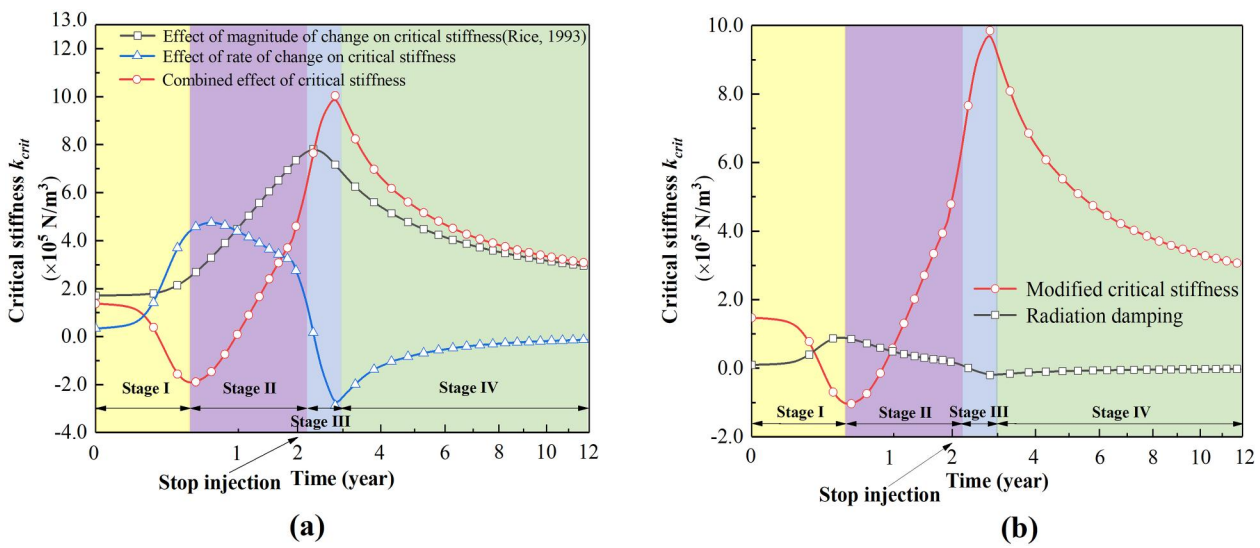

Figure 5. Components that affect the evolution of critical stiffness in response to CO_2 injection. (a). Evolution of the effect of the magnitude of the effective stress, the rate of change of the effective stress, and the combined effect of both elements on critical stiffness. (b). Evolution of modified critical stiffness and the effect of radiation damping.

As illustrated above, the joint impact of both effective stress magnitude and rate of change fluctuates during the full CO_2 injection period, as shown in Figure 5a. The rate of change in effective stress plays a major role both at the initial stage of injection and its end, as shown in the first and third stages of Figure 5a. Conversely, effective stress magnitude controls the evolution of the critical stiffness as the effective stress approaches the steady state, as shown in the second and fourth stages of Figure 5a.

4.1.3. Impact of Radiation Damping on Critical Stiffness

The impact of radiation damping on the critical stiffness of the fault in the above four stages is illustrated in Figure 5b. (a) In the first stage, both the effective stress and its rate of change in the fault core increase sharply, with the latter playing the dominant role. As displayed in Equation 13, the impact of radiation damping, $\xi\left[\frac{(\dot{\sigma_n}-\dot{p})}{(\sigma_n-p)}-\frac{v_0}{d_c}\right]$, is directly proportional to the effective stress rate and is inversely related to the effective stress magnitude. Under this condition, radiation damping increases the critical stiffness. (b) In the second stage, the increment of pore pressure decreases, which reduces the enhancement from the confinement effect in the fault core, and thereby the rate of increase of effective stress decreases but remains positive. Therefore, radiation damping still increases critical stiffness, but at a lower rate compared to that within the first stage. (c) In the third stage, the effective stress on the fault core decreases sharply when injection stops, and fluid diffuses further into the reservoir—resulting in a negative rate of change. In this stage, the decreasing rate plays the decisive role and increases the critical stiffness, with radiation damping reducing the critical stiffness, thereby pushing the system toward an aseismic response to fault slip. (d) In the fourth stage, effective stress continues to decrease with a negative rate of change that approaches zero as the extrusion effect further decreases. As shown in Figure 5b, radiation damping reduces the critical stiffness that stabilizes the fault, but at a slower rate compared with that in the previous stage.

4.1.4. The Likelihood of Occurrence of Seismic Slip

In the previous, the value of $\tau - \tau_p$ is first checked to determine whether the fault is reactivated during fluid injection. As noted above, the value is initially negative as fluid injection begins and then transits to a positive value with continuous injection which is maintained positive for some time, even as injection stops. In other words, the fault could be reactivated both during the stage of continuous fluid injection and after a pause in injection. Then the evolution of the critical stiffness in the fault core is followed to define fault slip mode—again divided into four stages: (a) In the first stage of CO_2 injection, the increasing rate of change in effective stress plays the main role in decreasing critical stiffness, whereas the inhibition effect of radiation damping enhances critical stiffness, as shown in the first stage of Figure 5b. (b) In the second stage, critical stiffness increases due to the enhanced effective stress, and radiation damping increases critical stiffness, as shown in the second stage of Figure 5b. (c) Once injection ceases, critical stiffness is enhanced, as controlled by the decreasing rate of change in effective stress, while the impeding effect of radiation damping reduces critical stiffness, as shown in the third stage of Figure 5b. (d) Finally, critical stiffness decreases due to the reduction in effective stress, and the effect of radiation damping reduces critical stiffness, as shown in the fourth stage of Figure 5b. The net impact of these effects (magnitude of effective stress, rate of change in effective stress and radiation damping) on critical stiffness thus decreases rapidly in the first stage of injection, then first increases in the second stage, before rapidly increasing in the third stage, and finally decreasing slowly to a constant in the fourth stage. Summarizing these mechanistic observations, the fault could be reactivated during the stage of continuous fluid injection—the second stage in this case—while seismic slip is most likely to occur after the fluid injection suddenly stops.

4.2. Effect of Engineering Factors on Fault Response

We next examine the impacts of different injection scenarios, relative locations of the injection wells and locations related to the faults on the evolution of critical stiffness—and hence on the propensity and the likelihood for seismic slip.

4.2.1. Evolution of Critical Stiffness With Different Injection Strategies

In order to explore the potential impact of CO_2 injection strategy on the likelihood of seismic slip, as evaluated through anticipated evolution of critical stiffness, a total of four injection schedules are designed based on

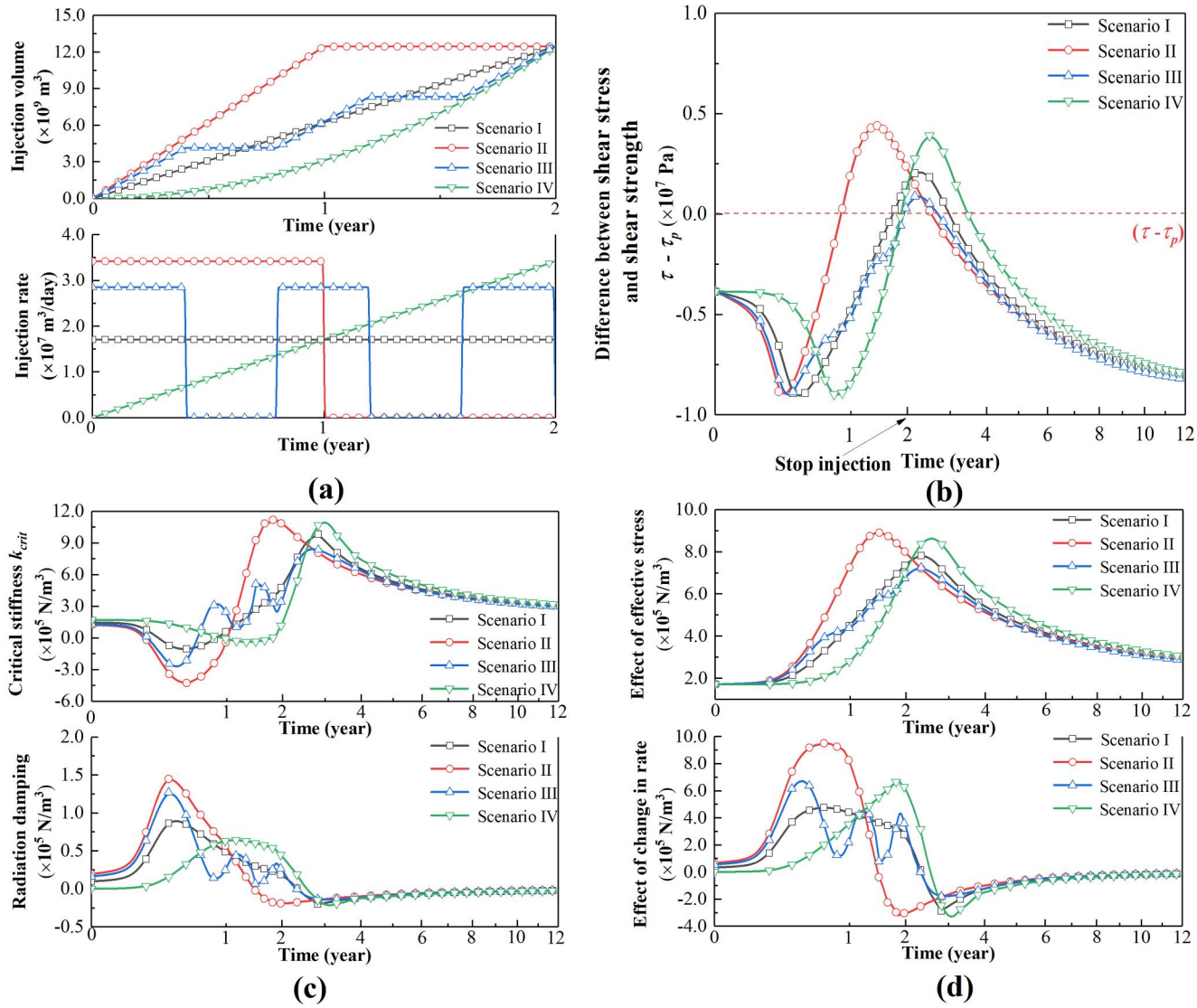

Figure 6. Comparison of stability profiles from four different injection scenarios. (a). Injection volume and injection rate. (b). Difference between shear stress and peak shear strength. (c). Critical stiffness and radiation damping. (d). Magnitude and rate of change in effective stress.

variation in injection rates. These are: I. Constant injection (Scenario I, the benchmark model); II. Constant injection with a doubled injection rate over half of the previous injection period (Scenario II); III. Cycling injection (Scenario III), and IV. Linear increase in the injection rate (Scenario IV). The injection rate and total volume of the four injection cases are shown in Figure 6a, in which the total injection volumes of Scenarios I, III, and IV are identical at the end of 2 years and for Scenario II the time is 1 year because of its doubled injection rate. All injection scenarios (mentioned above) are followed by a 10-year shut-off period after a 1- or 2-year duration of injection.

As illustrated in Figure 6b (Figure 6, and Figure S1 in Supporting Information S2), all of the four injection cases tend toward fault reactivation as the shear stress of the fault is greater than its peak frictional strength during the injection process. When comparing Scenarios I and II (Figures 6c and 6d), we reach several conclusions: (a) When the injection rate suddenly changes (i.e., injection starts and stops), the critical stiffness of the fault and the effect of radiation damping in Scenario II vary more dramatically compared with those in Scenario I, since doubling the injection rate in Scenario II produces a greater perturbation in the critical stiffness. (b) During the constant injection stage and the self-equilibrating stage, the increasing and decreasing stages of critical stiffness in Scenario II are more significant than those in Scenario I due to the greater variation

in effective stress in the fault core. (c) Furthermore, the impact of radiation damping on the critical stiffness decreases and then increases more clearly in Scenario II. In summary, the critical stiffness of the fault in the case of Scenario II varies more dramatically than that of Scenario I during the entire injection and self-equilibration stage. The critical stiffness and the effect of radiation damping in Scenario III pass through the three cycles during cycling injection (on-off-on). In the first two cycles, the critical stiffness in Scenario III is greater than that in Scenario I due to the greater injection rate. For the final cycle, the value of critical stiffness is lower compared with that in Scenario I due to the decline in the changing rate in effective stress during the injection pause relative to the first two cycles lowering the critical stiffness, as indicated in Figures 6c and 6d. The effect of radiation damping on the critical stiffness in all cycles in Scenario III is always greater than that in Scenario I.

Figure 6c demonstrates that the likelihood of injection-induced earthquakes evolves with the duration of the injection period for a fixed total injected volume. We observe that the likelihood of an earthquake depends on the duration of injection and is expressed by the peak value of critical stiffness (Alghannam & Juanes, 2020). The critical stiffness decreases as injection suddenly begins, and increases with injection time, thus increasing the likelihood for seismicity and potentially triggering earthquakes. When comparing Scenarios I, III, and IV, Scenario IV is the most likely to result in seismic fault reactivation, as demonstrated by the fact that it has the largest critical stiffness. At early injection times, the rate of change in effective stress in Scenario IV is the lowest because it has the smallest injection rate, but this rate of change increases linearly with increasing injection time. When injection stops, the greatest magnitude of critical stiffness is obtained in Scenario IV, and the inhibiting effect of radiation damping is the greatest since it hosts the largest rate of decreasing effective stress. Overall, the maximum value of the critical stiffness of the fault with a linear injection rate (Scenario IV) is the greatest, followed by that of constant injection (Scenario I) and finally, by that of cycling injection (Scenario III). Injecting CO_2 at a cycled injection rate is a relatively safe injection strategy. Moreover, the critical stiffness of the fault with a doubled injection rate (Scenario II) reaches the extremum value faster and is most likely to be unstable compared with that in Scenarios I, III, and IV. In summary, for a fixed total injected volume, a higher injection rate—or a linear injection-rate strategy—results in a greater likelihood of triggering unstable slip.

4.2.2. Evolution of Critical Stiffness With Different Injection-Well Positions

The distance between the injection well and the fault is also varied (1.0, 1.5, and 2.0 km, Figure 7a) to illustrate the impact of the location of the injection well, relative to the fault, on the evolving critical stiffness of the fault core. As illustrated in Figure 8a (and Figure S2 in Supporting Information S2), the reactivation of the fault occurs more readily with a closer injection well, featuring the earliest appearance time of $\tau - \tau_p = 0$ and largest value of $\tau - \tau_p$. The critical stiffness of the fault core with proximal injection varies more dramatically when the injection abruptly starts and then stops as displayed in Figures 8b and 8c. Additionally, the radiation damping in the case of a closer injection well exerts a greater effect on the critical stiffness of the fault core. In the injection stage, the critical stiffness and radiation damping effect change faster for a fault core with a closer injection, due to the larger increment in effective stress in the fault core. Conversely, when injection stops, the critical stiffness of the fault core, for the case of a closer injection well, reaches its maximum earlier with a greater inhibition due to the larger radiation damping term. Thus, the critical stiffness of the fault core with a close injection well decreases more conspicuously and reaches its minimum value in the early stages of the injection. Subsequently, the critical stiffness increases significantly when a greater increment of effective stress in the fault core exerts the most unstable effect on the fault and thus potentially drives seismic slip.

4.2.3. Evolution of Critical Stiffness Along the Fault Under Different Injection Well Locations

We next consider a case in which the injection well has been set in either the hanging wall or the footwall of the fault with the same distance to the fault to investigate the response at different positions of the fault to CO_2 injection. Three locations at different elevations along the dip of the fault are selected for comparison and position "B" refers to -the intersection of the fault and the reservoir (monitoring area in other cases), with positions "A" and "C" being located 50 m above and below the monitoring area, respectively (Figures 7b and 7c). In both cases —injection wells located either in the hanging wall or footwall of the fault—all three positions exhibit reactivation behavior which occurs earlier at positions "A" and "C" as illustrated in Figures 9a and 9b (and Figure S3 and S4 in Supporting Information S2). The largest discrepancy is that location "C" generates the largest value of τ

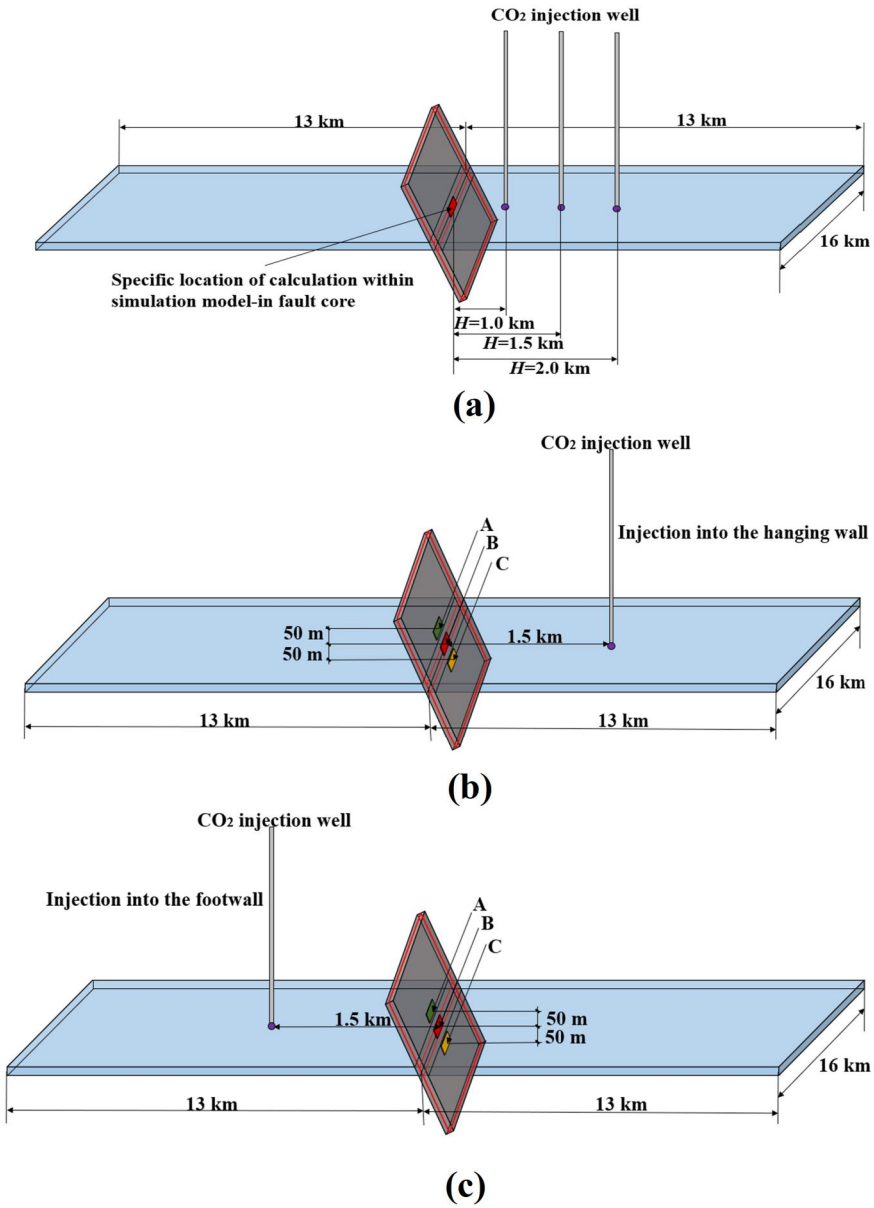

Figure 7. Cases of a fault with different positions of the injection well relative to the fault. (a). Three cases of different injection-well locations. (b). Different positions on the fault under the condition of injection into the hanging wall. (c). Different positions on the fault under the condition of injection into the footwall.

$-\tau_p$ when injected into the hanging wall, and conversely the largest value is obtained in position "A" when injected into the footwall. Also as shown in Figures 9c–9f, location "B" (i.e., the junction between the fault and the reservoir) in the fault core is characterized by the most dramatic variation in both critical stiffness and the radiation damping effect, irrespective of whether injection is conducted into the hanging wall or the footwall. In addition, the critical stiffness at location "A" in the fault core varies more dramatically than that at location "C" during injection into the hanging wall (Figures 9c and 9d) and also demonstrates a greater impact of radiation damping on critical stiffness. Conversely, the critical stiffness at location "C" in the fault core varies more dramatically than that at location "A" for the case of injection into the footwall (Figures 9e and 9f). The critical stiffness at location "B" in the fault core exhibits the greatest reduction compared with locations "A" and "C" in the early injection stage. While later the critical stiffness at location "B" increases with increasing injection time and achieves a maximum value and most unstable state, thereby making the area more likely to induce unstable fault slip.

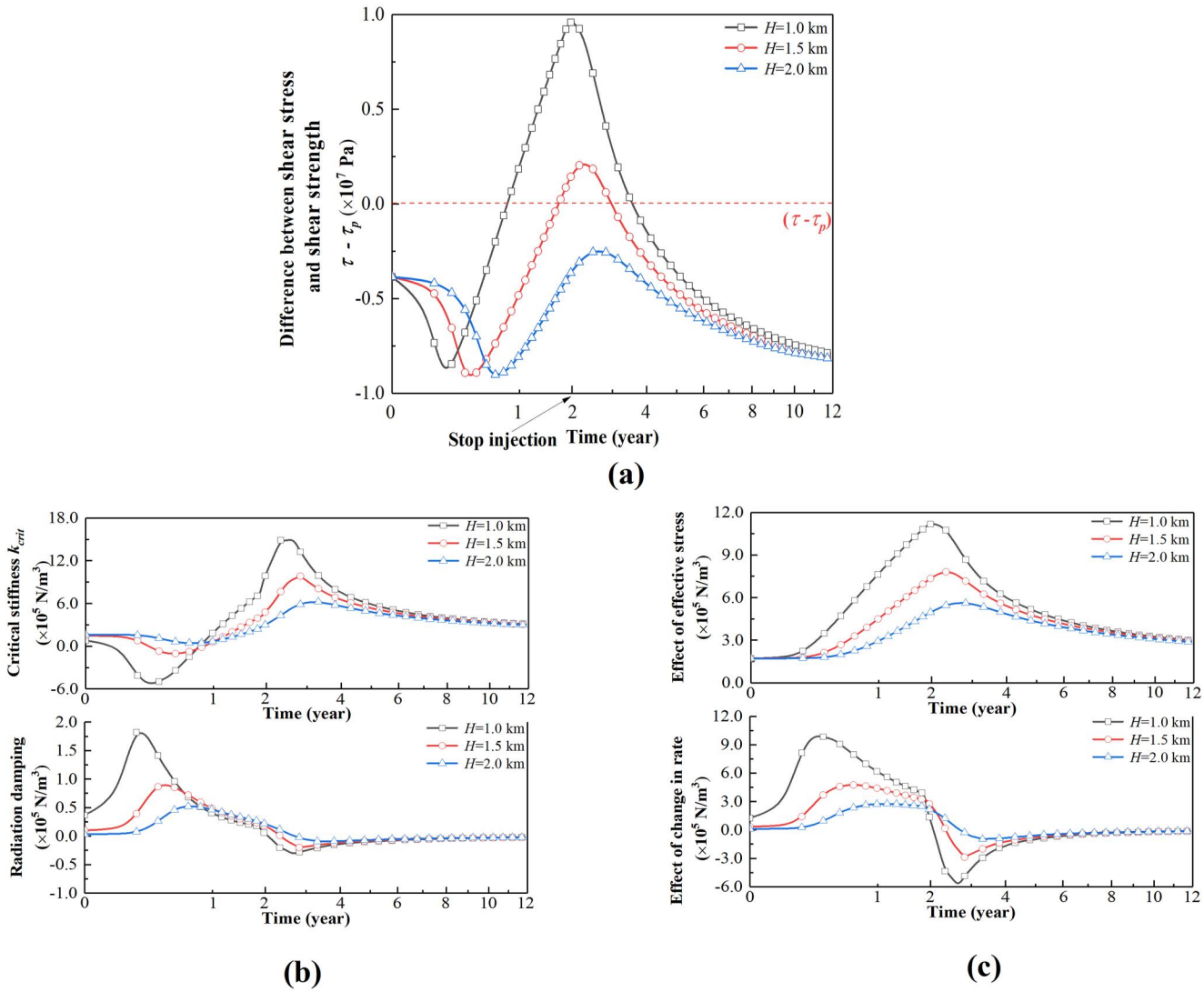

Figure 8. Comparison of stability profiles for three different injection-well sites. (a). Difference between shear stress and peak shear strength. (b). Critical stiffness and radiation damping. (c). Magnitude and rate of change in effective stress.

4.3. Effect of Hydrogeological Factors on Fault Response

We now examine the impact of permeability within the reservoir and in situ stresses on the evolution of critical stiffness.

4.3.1. Evolution of Critical Stiffness Under Varied Reservoir Permeabilities

CO_2 is most likely to be stored in a variety of different strata, such as in depleted oil reservoirs, deep saline aquifers, and unmineable coal seams (Sliaupa et al., 2013). Indeed, reservoirs with a broad variety of permeabilities are likely encountered (Liu et al., 2018; Vivek & Kumar, 2019). Under a constant injection rate, an analysis of comparative results with varied permeability can therefore guide site selection for CO_2 storage. As shown in Figure 10a (and Figure S5 in Supporting Information S2), reservoirs with a greater permeability are less prone to fault reactivation since fault shear strength will remain greater than the shear stress. Reactivation is more likely in reservoirs with lower permeability.

Figures 10b and 10c demonstrate that a fault embedded in a high permeability reservoir returns a shorter response-time to fluid injection and a lower level of critical stiffness compared with cases of low permeability. Conversely, a fault embedded in a low permeability reservoir is characterized by greater critical stiffness because of the stress

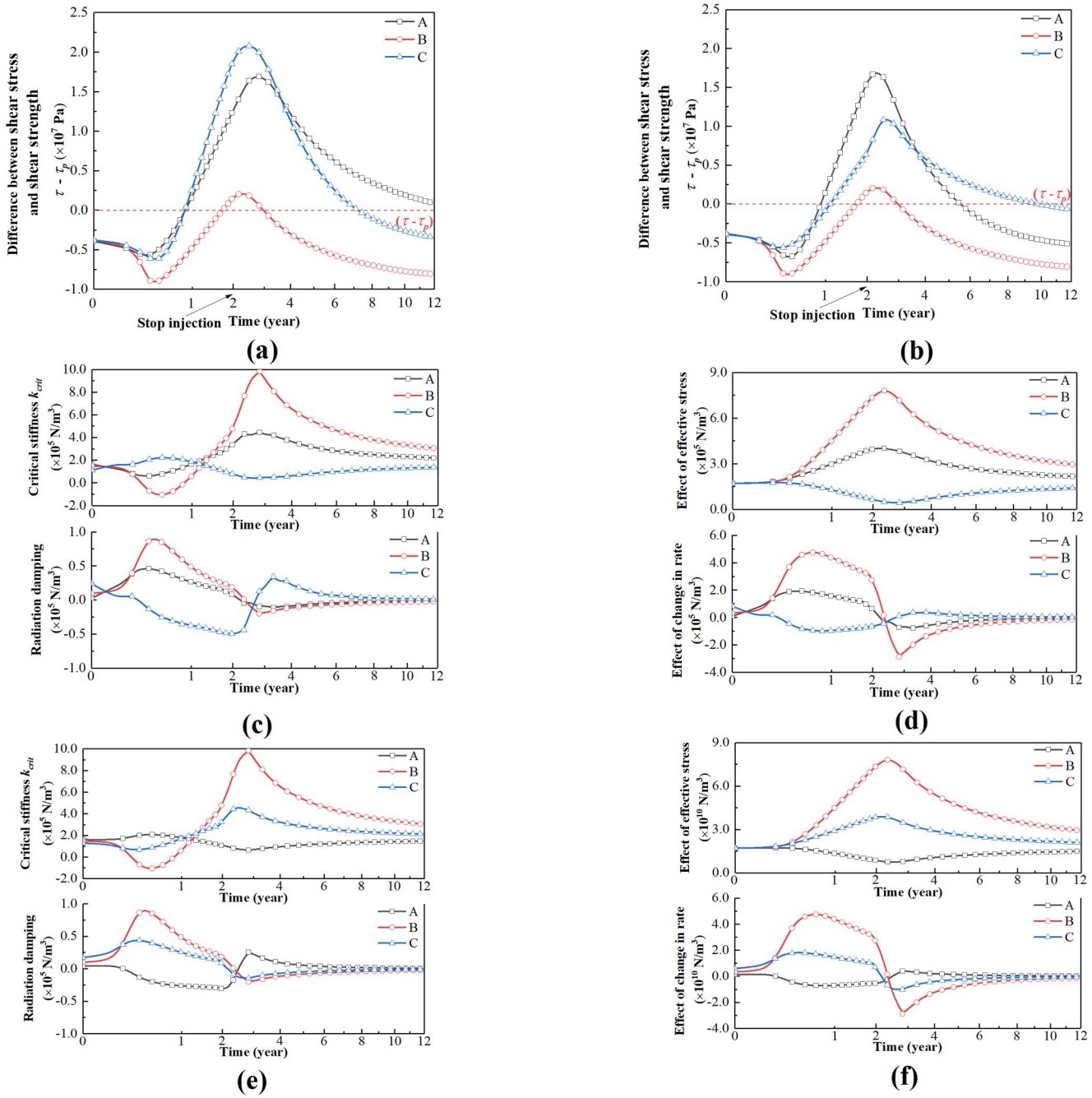

Figure 9. Comparison of stability profiles for different fault positions. (a). Difference between shear stress and peak shear strength for the case of injection into the hanging wall. (b). Difference between shear stress and peak shear strength for the case of injection into the footwall. (c). Critical stiffness and radiation damping for the case of injection into the hanging wall. (d). Magnitude and rate of change in effective stress for the case of injection into the hanging wall. (e). Critical stiffness and radiation damping for the case of injection into the footwall. (f). Magnitude and rate of change in effective stress for the case of injection into the footwall.

concentration and lower radiation damping effect. In the initial stages of CO_2 injection, critical stiffness in the fault core decreases faster in the case of a higher permeability reservoir and the impact of radiation damping on critical stiffness increases more rapidly. When injection ceases, the critical stiffness in the fault core within the lower-permeability reservoir increases more significantly and is characterized by lower inhibition of radiation damping due to the greater effective stress. Therefore, under a constant injection rate, the lower the permeability of the reservoir, the greater the maximum value of the critical stiffness of the fault. In summary, reservoirs with lower permeability have a greater likelihood of triggering seismic fault slip.

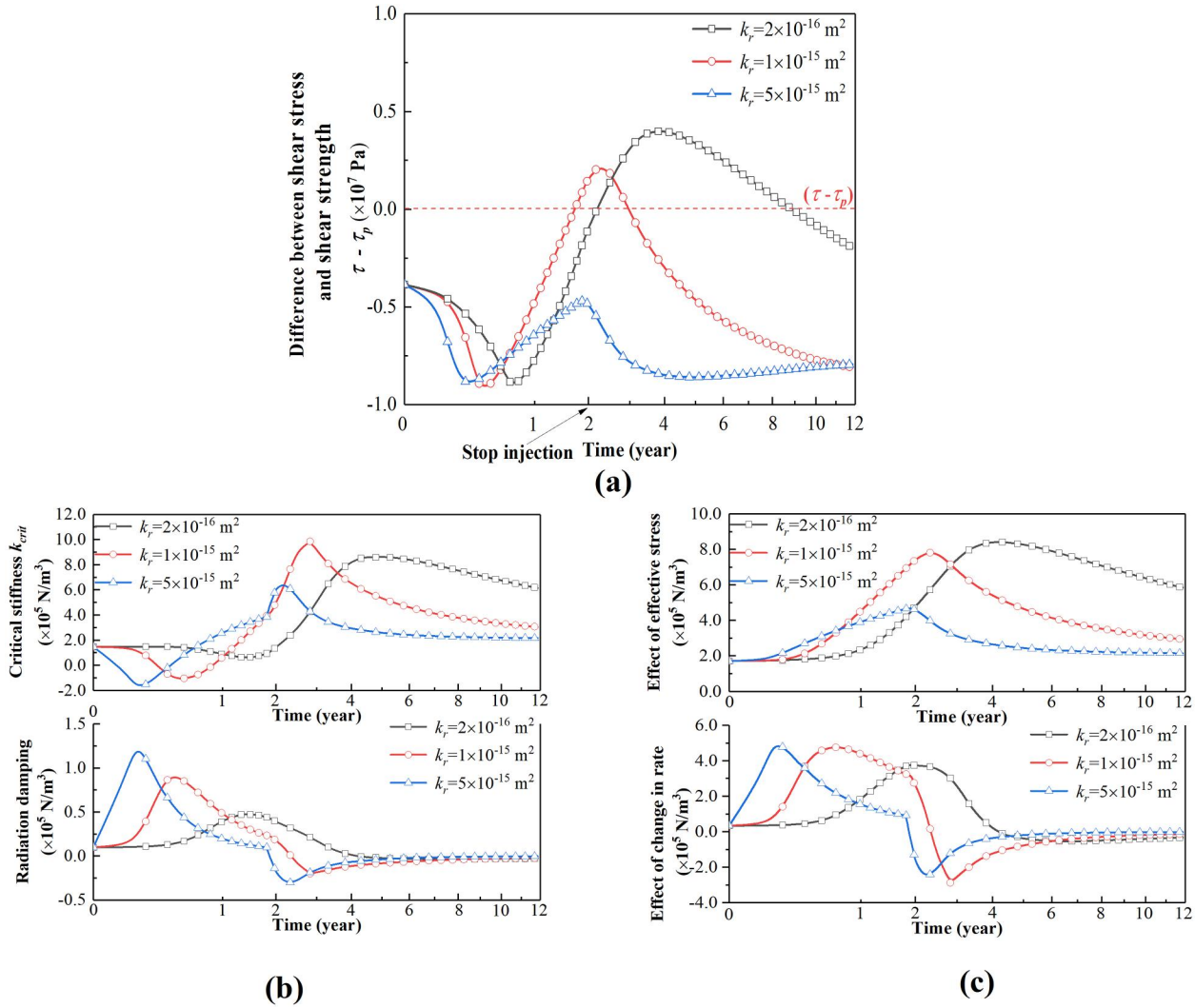

Figure 10. Comparison of stability profiles for different reservoir permeabilities. (a). Difference between shear stress and peak shear strength. (b). Critical stiffness and radiation damping. (c). Magnitude and rate of change in effective stress.

4.3.2. Evolution of Critical Stiffness Under Different In Situ Stress Conditions

Three faulting regimes—normal faulting ($\sigma_v \geq \sigma_x \geq \sigma_y$), reverse faulting ($\sigma_y \geq \sigma_x \geq \sigma_v$), and strike-slip faulting ($\sigma_x \geq \sigma_v \geq \sigma_y$) as defined by Andersonian stress regimes (Anderson, 1905)—are designated to investigate injection-induced instability under different fault habits and in situ stress conditions. To achieve this, here, we specify the value of σ_v as a constant and adjust the magnitudes of σ_x and σ_y to generate the three contrasting fault regimes. The initial stress values for the three fault regimes are summarized in Table 2 and allow faults to be optimally oriented for slip. The distances between the injection well and the fault core are the same for all three fault regimes.

As shown in Figure 11a (and Figure S6 in Supporting Information S2), the three fault regimes have similar initial shear and normal stresses on the fault and also trends in variation of both terms. Also, the fault would slip for all three regimes as the difference between shear stress and peak frictional strength of the fault core is positive during the injection period (Figure 11a). Then we calculate the evolution of critical stiffness to evaluate the likelihood of seismic slip. It should be noted that the ratio of critical stiffness (k_{crit}/k_0, k_0 denotes the value of critical stiffness in the initial state) is used diagnostically. Because the various stress regimes result in different initial values of critical stiffness—the possibility of inducing fault stick-slip differs—thus we aim to normalize them to compare the response of different fault regimes to the same fluid injection scenario. As shown in

Table 2
Stress Conditions for Different Fault Regimes

Stress regime	σ_v (Pa)	σ_x (Pa)	σ_y (Pa)	Fault strike
Normal faulting	2.5×10^7	2.0×10^7	1.7×10^7	Parallel to σ_x
Reverse faulting	2.5×10^7	2.8×10^7	3.0×10^7	Parallel to σ_x
Strike-slip faulting	2.5×10^7	3.1×10^7	2.1×10^7	30° to σ_x

Figure 11b, the variation in the critical stiffness ratio for reverse faulting is the greatest, followed by normal faulting and finally for strike-slip faulting. The change in stiffness ratio due to radiation damping and effective stress are also shown in Figures 11b and 11c. Strike-slip faulting exhibits the smallest change in the ratio and the lowest effect of radiation damping while reverse faulting shows the opposite trend. In summary, the evolution of the critical stiffness ratio in the case of reverse faulting varies most significantly and should be most likely to transition to seismic fault slip.

5. Model Verification and Discussion

5.1. Explanation of Experimental and Field Observations

5.1.1. Explanation of Experimental Observations

Laboratory injection-induced fracture stick-slip data (Wang et al., 2020)—presented in Figure 12a–can be used to gain insight into mechanisms of injection-induced unstable slip of fault (the experimental setup is displayed in Figure S7 in Supporting Information S2 (Wang et al., 2020)). Results from this particular

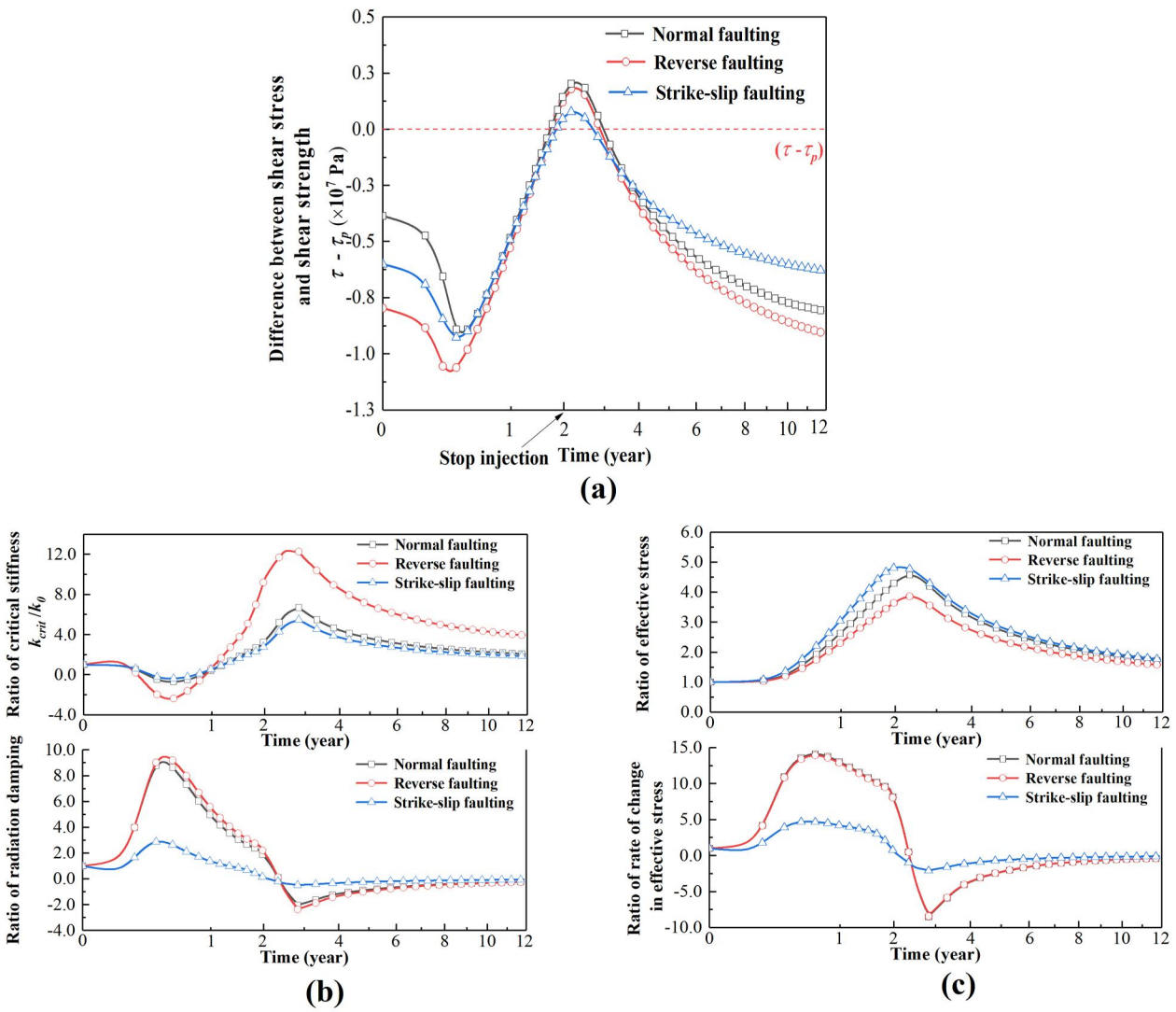

Figure 11. Comparison of stability profiles for the three different faulting regimes. (a). Evolution of shear stress, peak shear strength and their difference. (b). Ratio of critical stiffness and radiation damping. (c). Ratio of effective stress and rate of change in effective stress.

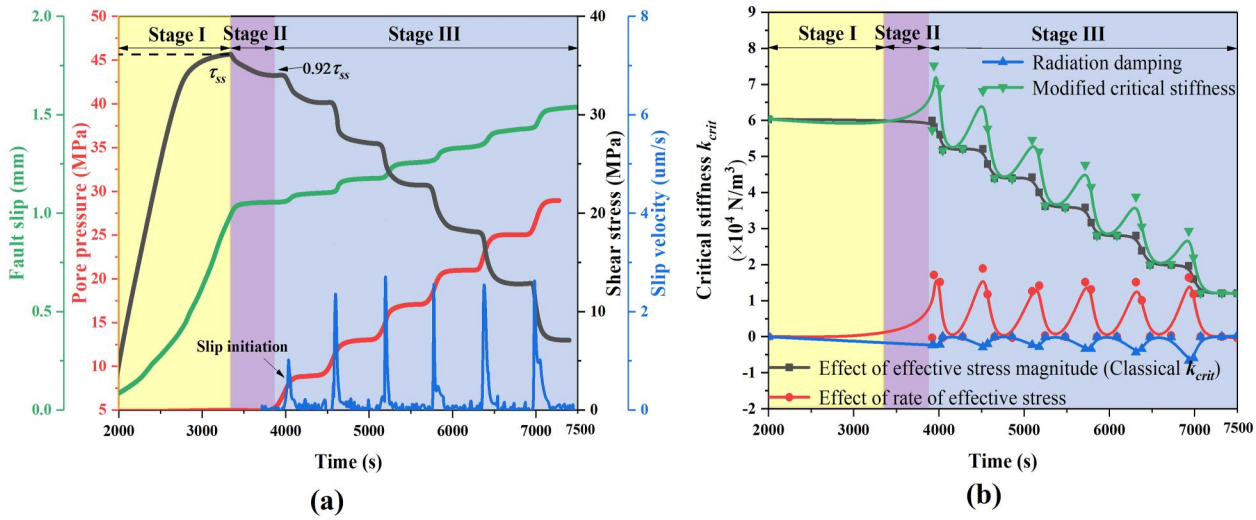

Figure 12. Laboratory injection induced fault slip data and calculated critical stiffnesses (a). Evolution of pore pressure, shear stress, slip velocity and fault slip distance over time in an injection-induced fault stick-slip experiment (Wang et al., 2020). The green curve represents the evolution of the fault slip distance, the black curve represents the evolution of the shear stress, the blue curve represents the evolution of the slip velocity, and the red curve represents the evolution of the pore pressure. (b). Components that affect the evolution of critical stiffness in response to the injection-induced fault stick-slip experiment. Among them, the value of friction parameters ($b-a$) is 0.2, the characteristic slip distance is 1.0×10^{-4} m, the initial slip velocity is 1.0×10^{-6} m/s and the normalized frictional parameter is 0.5.

experiment can be divided into three stages. In Stage I, shear strength at steady state was reached through increasing the driving stress then reduced to ~0.92 τ_{ss} for Stage II. Fluid pressure was then applied to the sample at a fluid pressurization rate of 2 MPa/min in Stage III. As illustrated in Figure 12a, increasing fluid pressure under constant normal stress results in unstable slip characterized by a sudden increase in slip velocity. We can calculate the changes in critical stiffness with both classical and modified models to predict the likelihood of triggering earthquakes. In the validation process, the coefficient of radiation damping ξ is defined as 1.0×10^2 Pa/(m/s). Also, the fault state parameters v_0 and the friction parameter d_c are defined as 1.0 μm/s and 1.0 mm, respectively. The value of the stability parameter ($b - a$) is 0.2 and the frictional coefficient is 0.5. In the experiment of Wang et al. (2020), fluid pressure was incremented in six sub-stages (Figure 12a) with unstable slip observed for each stage, which can be treated as an individual isolated event. Figure 12b illustrates the evolution of critical stiffness over the entire experiment with two stages observed over each pressure increment: an increasing stage at early time and a decreasing stage at late time. The second seismic event is taken as an example to illustrate how the critical stiffness (k_{crit}) can be applied to indicate the likelihood of seismicity. As the fluid pressure suddenly increases, the critical stiffness rapidly rises to its maximum value and then reduces with injection time until the next incremented cycle. Therefore, a peak value can be observed in each incremented pressure cycle with its value larger than that during the decremented phase in the former stage. These characteristics suggest that the increase in injection rate can increase the critical stiffness and increase the likelihood of triggering seismic slip. Thus, the likelihood of induced seismic slip can be inferred from the value and direction of change of the critical stiffness. In summary, the maximum value of critical stiffness, indicating the greatest likelihood of inducing unstable slip, is achieved when the pore pressure suddenly increases for each cycle. That is to say, the stage in which critical stiffness increases sharply is the stage that is most likely to induce instability of the fracture and to therefore drive seismic slip. Also, the impacts of magnitude and rate of change in effective stress are shown in Figure 12b. The conclusion is that a dramatic increase in the rate of change in effective stress is the main contributor to the increase in the critical stiffness.

Furthermore, the competition between the absolute magnitude and rate of change in effective stress, in impacting the critical stiffness of the fault, is also qualitatively consistent with other laboratory observations (French et al., 2016), which indicate that changing stress rate plays a crucial role in slip mode during the early stages of fluid injection. Similarly, Byerlee (1970) notes that the sliding between two rock surfaces is more stable at low rather than at high effective stresses with injection evolving from initial to steady-state conditions. This observation could be explained by the notion that the evolution of critical stiffness

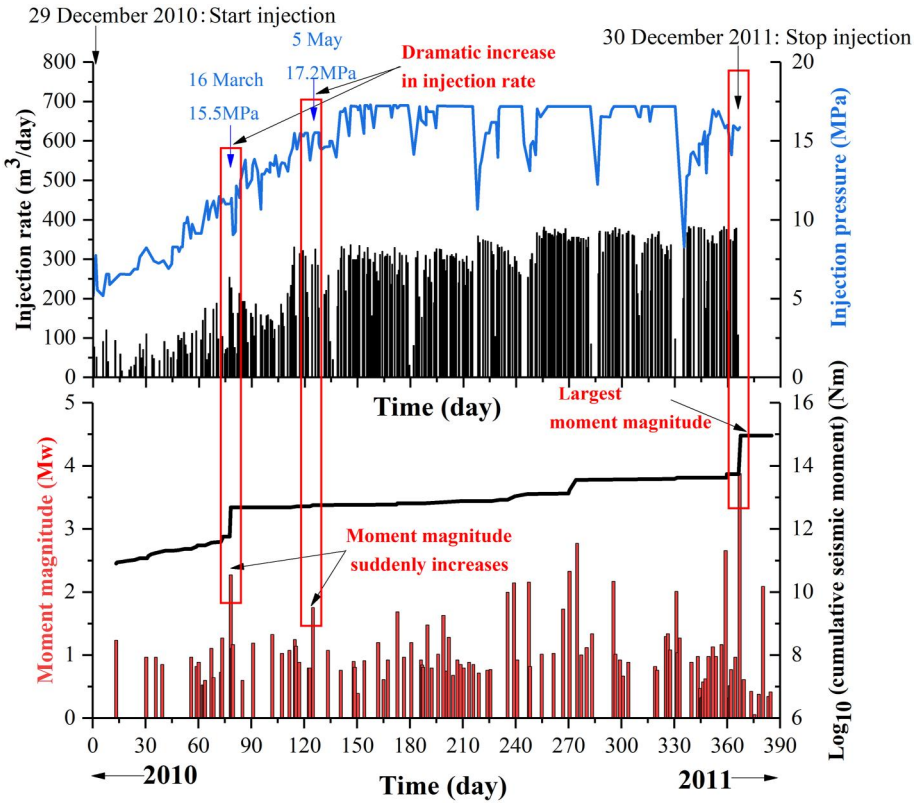

Figure 13. Injection pressure and daily injection volume at the NorthStar 1 well, including the moment magnitude and the cumulative moment of all detected seismic events near the well (Kim, 2013).

is mainly dominated by effective stress magnitude in the late-time equilibration stage and a lower effective stress leads to a smaller value of critical stiffness - representing the evolution of the system toward stability.

5.1.2. Explanation of Field Observations

Numerous seismic events with moment magnitudes ranging from 0.4 to 3.9 have been monitored close to a deep-fluid-injection site in Youngstown, Ohio (Kim, 2013). Figure 13 displays the injection pressure, the daily injection volume, injection rate, and the moment magnitude (M_w) of the seismic events as well as the cumulative moment of all detected seismic events from December 2011 to January 2012.

As observed in Figure 13, a sudden increase in moment magnitude often follows a rapid on-off-on in injection rate (e.g., 16 March 2010 and 3 May 2010). This correlation between seismic moment magnitude and injection rate can be explained by the proposed critical stiffness criterion in this work. The impact of the reduction of the injection rate may not be detected by the field monitoring due to the short duration of the shut-off of the injection and the value of the critical stiffness first decreases and then increases to its maximum value with each increment of the injection rate. Thus, the correlation between seismic moment magnitude and injection rate in the field can be explained by the notion that the critical stiffness should increase and promote earthquakes as the injection rate suddenly increases. Additionally, another discovery in the field is that the greatest seismic event occurred after injection had stopped on 30 December 2010, instead of during the injection stage. As indicated in the proposed model (Equation 13) and Figure 6 (a), critical stiffness would increase because of the decreasing rate of change in effective stress when the injection rate suddenly declines. Thus, the maximum value of the critical stiffness always occurs after the injection rate has decreased over a period of time, which represents the most unstable case.

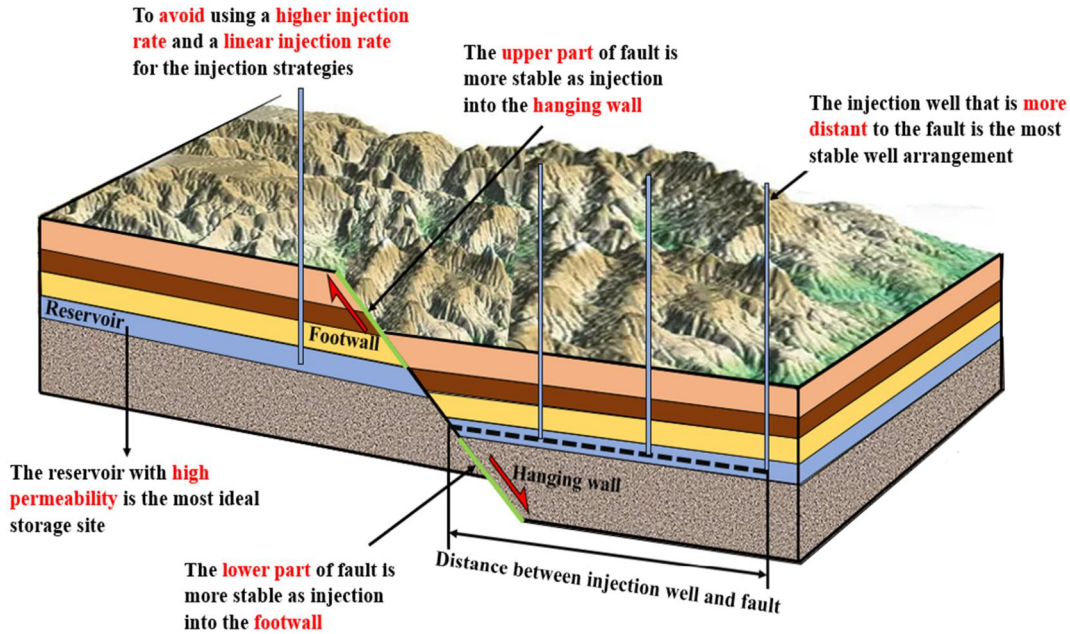

Figure 14. Illustrated schematic overview of fluid injection.

5.2. Discussion

5.2.1. Impact of Inherent Parameters on the Critical Stiffness

In the above sections, the impacts of both operational and hydrogeological factors on the critical stiffness are characterized. In addition to these factors, the critical stiffness is also dominated by the friction parameters—$(b-a)$, d_c, α and fault state parameters ξ, v_0. The former can be obtained through single/double direct shear experiments with the latter recovered from field observations. In the modified equation, the critical stiffness is characterized by three terms—magnitude of effective stress, rate of change in effective stress and radiation damping. Variations in these friction and fault state parameters control the evolution of effective stresses and radiation damping: (a) The value of $(b-a)/d_c$ directly determines the magnitude of effective stress contributing to the critical stiffness with a larger $(b-a)$ or a smaller d_c resulting in a more significant role of the magnitude of effective stress; (b) Similarly, the contributing proportion of the rate of change in effective stress is mainly dominated by the value of $-\alpha/v_0$ with a larger contribution observed for a larger α or a smaller v_0; (c) Slightly more complex is the role of the radiation damping term. Its proportion in the total critical stiffness depends on the value of ζ which characterizes the recurrence interval periods of earthquakes. A higher ζ represents a shorter recurrence interval and leads to a larger contribution of the radiation damping term. Furthermore, the radiation damping term consists of two components—one results from the disturbance due to fluid injection and the other is an inherent property of the fault. When the value of v_0/d_c is large, the latter item plays a dominant role and vice versa.

Summarizing the impact of each parameter on three terms: (a) The value of $(b-a)$ is only positively related to the proportion of the magnitude of effective stress, (b) d_c impacts the contributions of magnitude of effective stress and fluid injection on radiation damping in a negative way, (c) Initial slip velocity v_0 shows a negative correlation with the proportion of the change rate in effective stress, while a positive correlation with the injection rate in radiation damping. Another point to be aware of is that in the classical critical stiffness equation a positive magnitude of the parameter $(b-a)$ is essential for seismic slip. While in the modified equation in this work, this condition is not necessarily required as the rate of change in effective stress could also change the sign of critical stiffness when the value of α/v_0 is sufficiently large.

5.2.2. Field Guidance

A series of parameter-sensitivity analyses are conducted in order to guide the site selection of CO_2 geological sequestration. Some helpful suggestions can be given based on the numerical results. A schematic illustration

(Figure 14) is shown in order to provide guidance for CO_2-storage projects: (a) For a fixed total injection volume, a cycled injection rate is the most stable injection strategy for CO_2 geological storage. The strategies of using a higher injection rate and a linear injection rate can both potentially trigger earthquakes, which should be avoided; (b) A high-permeability reservoir is most suitable for subsurface injection engineering because it is difficult to generate significant pressure accumulation in a reservoir during the process of CO_2 injection into the reservoir; (c) Well locations that are most distant from the fault are preferred; (d) Injection into a reverse faulting regime is the most unstable and unsuitable method of CO_2 storage compared with normal faulting and strike-slip faulting; (e) Experiments and field characterization should be conducted to determine the inherent parameters contributing to critical stiffness—$(b - a)$, d_c, α and ξ, v_0, and furthermore estimate the contribution of each term to the total critical stiffness; (f) Furthermore, a negative value of the parameter $(b - a)$, that is $(b - a) < 0$, does not necessarily guarantee stable slip as demonstrated in our proposed model, where an abrupt negative rate in effective stress may increase the value of critical stiffness and change its sign from negative to positive, due to the fluid pressure build up or poroelastic effects.

5.2.3. Comparison With Previous Works

Although Rice (1993) introduced a damping term, the derived critical stiffness or critical nucleation length did not contain the damping effect. Rice (1993) determined the slip histories along a planar vertical fault embedded within an elastic half-space and explored the complex relationships between slip with computational element size. Radiation damping was only introduced in the shear stress equation (governing equation) to govern the slip characteristics of the fault. A nucleation size was proposed to specify the computational element size. To define the nucleation size, the classical critical stiffness was employed, which does not include a radiation damping term. In this model there was an inconsistency in considering the damping term in the classical critical stiffness and the governing equation.

Thus, this prior work (Rice, 1993) mainly focused on the impact of the ratio of element size to critical size on the spatio-temporal complexity of slip on a fault. Therefore, it was sufficient to employ the classical critical stiffness to approximately estimate the minimum diameter of a patch of faults developing unstable slip. However, recent field observations suggest that changing injection rates always correlate with increased occurrences of induced earthquakes (e.g., Healy et al., 1968; Improta et al., 2015; Langenbruch & Zoback, 2016). Changes in injection rates generally precede the occurrence of earthquakes (Kim, 2013; Tang et al., 2018)—and the classical critical stiffness criterion concept cannot explain these observations. To investigate the effect of injection rate on the likelihood of injection-triggered seismicity, Alghannam and Juanes (2020) proposed a modified critical stiffness model. Only the impact of rate of change in the pore pressure was considered. In this work, we further modify the critical stiffness criterion by considering the impact of change rate in effective stress and that of radiation damping.

5.2.4. Limitations and Future Work

In previous studies, critical stiffness had been used to estimate the likelihood of triggering injection-induced earthquakes by considering the magnitude of effective stress and the rate of pore pressure of fault. However, the rate of change in normal stress on a fault that results from fluid injection has been largely ignored and inertial effects, which are characterized by radiation damping, have not been considered in the evaluation of the critical stiffnesses of faults. In the present work, we propose a modified critical stiffness criterion that considers the effect of rate of change in effective stress (which includes pore pressure and normal stress) and the radiation damping of the fault. The contribution of each term—magnitude-of, rate of change in effective stress and radiation damping—can be quantified by the friction parameters—$(b - a)$, d_c, α and fault state parameters ξ, v_0. The frictional parameters (a,b,d_c) are also related to temperature while changes in temperature (Niemeijer & Spiers, 2007; Den Hartog & Spiers, 2014) and thermal stresses, although their combined impacts on rate-state response are not considered in our study. Furthermore, fault permeability is influenced by various factors, including structure, composition, and stress state. In addition, the fault damage zone is highly anisotropic in permeability with the maximum value observed in the direction parallel to the fault plane and parallel to the slip direction, followed by that parallel to the fault plane and perpendicular to fault slip and finally a minimum perpendicular to the fault (Farrell et al., 2014). Thus, the highly anisotropic nature of the fault damage zone should also be considered together with impacts of phase change and related temperature effects, which are of importance, for example, during the injection of CO_2 (Li, 2016).

Thus, future work should also consider CO_2-injection-induced fault slip experiments for investigating the elusive connection between fluid pressurization rates, friction parameters (a,b,d_c), radiation damping coefficient ξ, temperature effects and the behavior of induced fault slip. To achieve the above goal, small-scale fracture-slip-reactivation experiments that use fluid pressurization could serve as an analogy for large-scale fluid-injection-induced earthquakes (Li et al., 2021; Wang et al., 2020; Ye & Ghassemi, 2018). Stress regimes that are representative of faulting regimes—that is, normal, reverse, and strike-slip faulting—can be obtained by setting the initial stress state and sliding direction. An independent flow/pressure-control system can control rates and styles of pressure evolution on these laboratory faults. Also, temperature may be controlled to replicate the thermal environment of the reservoir. Using this approach, the effect of fluid pressurization rates, temperature and friction parameters on slip behavior in the varied faulting regimes can be investigated. Upscaling approaches that are similar to those used in this work would link the critical stiffness of the fault criterion between laboratory and field scales. Additionally, exploring the relationship between injection rates, induced earthquake magnitudes, seismic event moments and the energy stored in the fluid is meaningful to mitigate potential earthquakes by controlling pumping and well pressures in the field. It is also necessary to pay more attention to the analysis of monitored on-site seismicity data in future work (Kwiatek et al., 2019).

6. Conclusions

In the current study, a modified critical stiffness model is proposed to estimate the likelihood of injection-induced earthquakes during fluid injection. In this new model, critical stiffness is positively related to fault effective stress magnitude and negatively related to the rate of change in effective stress. Additionally, the inhibitory effect of radiation damping on critical stiffness is considered for the first time. The validity of the model is confirmed against both laboratory and field data. We consider a representative 3D geological model of a CO_2 injection reservoir with an embedded fault. A poromechanically coupled model is employed in the analysis which simultaneously links fluid-injection to fluid pressure and hence stress-re-distribution. The Mohr-Coulomb failure criterion is first employed to determine whether slip occurs on the fault. Then a modified critical stiffness is used as an index to estimate the likelihood of slip and its mode—stable or unstable. In this work, both geological factors viz. reservoir permeability, in situ stress state, and faulting regime, together with engineering factors viz. injection strategy and schedule and well location are investigated. The following conclusions are drawn.

1. Four stages are observed in the evolution of the fault critical stiffness during fluid injection. These stages evolve due to competition between the effects of effective stress magnitude and its rate of change. In addition, radiation damping also moderates fault critical stiffness. Initially, the combined effects of effective stress and radiation damping decrease critical stiffness and favor aseismic slip. Subsequently, both effective stress and the radiation damping increase the critical stiffness and favor seismic slip. When injection stops, the negative rate of change in effective stress decreases the radiation-damping effect and increases the critical stiffness. At final equilibrium, both effective stress and radiation damping decrease the critical stiffness and favor aseismic slip.
2. The rate of change in effective stress plays a dominant role when the injection rate suddenly changes. Conversely, the effective stress magnitude controls the variation of critical stiffness in both the constant injection stage and the self-equilibration stage. Critical stiffness reaches a minimum value upon the initiation of injection. A maximum value is reached after injection ceases, increasing the potential for the triggering of seismic slip. Seismicity does not occur immediately after injection has started or stopped with a time-lag observed that is dependent on reservoir permeability.
3. The impacts of the well field layout, injection schedules and various geological factors are all addressed. For the same volume of CO_2 injection, cycled injection is the most stable injection approach. A high permeability reservoir and large separation between the injection well and the fault are the best choices to minimize seismicity. A reverse faulting stress regime is the most unstable stress regime and is also the condition most likely inducing seismicity, where a dramatic variation in critical stiffness is observed.
4. Both the observations from: (a) injection-induced fault stick-slip experimental data and (b) the largest moment magnitude event generated after injection had stopped in the Ohio reinjection experiment, qualify the validity of the proposed model. However, fluid-injection-induced slip experiments are urgently needed to investigate the relation between fluid pressurization rates and frictional parameters (a,b,d_c).

Data Availability Statement

The Laboratory data used in this study for the Explanation of experimental observations are from the fault slip experiment study (Wang et al., 2020); The injection parameter and the detected seismic events used in this study for the Explanation of field observations are from the monitor data associated with fluid injection into a deep well in Youngstown, Ohio (Kim, 2013). Numerical modeling was carried out using COMSOL Multiphysics® (https://cn.comsol.com). The numerical data used for creating the figures in this paper is available for access via Harvard Dataverse (https://dataverse.harvard.edu/dataset.xhtml?persistentId=doi:10.7910/DVN/RZLPTY).

Acknowledgments
The authors would like to thank Prof. Xiating Feng, Prof. Chengxiang Yang, and Prof. Zaobao Liu from Key Laboratory of Liaoning Province on Deep Engineering and Intelligent Technology at Northeastern University for the faithful advice during the course of this research. DE acknowledges support from the G. Albert Shoemaker endowment. The authors would also like to thank the reviewers for their helpful reviews and suggestions. This work is funded by National Natural Science Foundation of China (12002081, 42374120), 402 Foundation of Earthquake Science (U1839207) and the 111 Project (B17009).

References

Aharonov, E., & Scholz, C. H. (2017). A Physics-based rock friction constitutive law: Steady state friction. *Journal of Geophysical Research: Solid Earth*, *123*(2), 1591–1614. https://doi.org/10.1002/2016JB013829

Alghannam, M., & Juanes, R. (2020). Understanding rate effects in injection-induced earthquakes. *Nature Communications*, *11*(1), 1–6. https://doi.org/10.1038/s41467-020-16860-y

Anderson, E. M. (1905). The dynamics of faulting. *Transactions of the Edinburgh Geological Society*, *8*(3), 387–402. https://doi.org/10.1144/transed.8.3.387

Anyim, K., & Gan, Q. (2020). Fault zone exploitation in geothermal reservoirs: Production optimization, permeability evolution and induced seismicity. *Advances in Geo-Energy Research*, *4*(1), 1–12. https://doi.org/10.26804/ager.2020.01.01

Atanackovic, T. M., & Guran, A. (2000). *Theory of elasticity for scientists and engineers*. Springer.

Biot, M. A. (1941). General theory of three-dimensional consolidation. *Journal of Applied Physics*, *12*(2), 155–164. https://doi.org/10.1063/1.1712886

Brace, W. F., & Byerlee, J. D. (1966). Stick-slip as a mechanism for earthquakes. *Science*, *153*(3739), 990–992. https://doi.org/10.1126/science.153.3739.990

Byerlee, J. D. (1970). The mechanics of stick-slip. *Tectonophysics*, *9*(5), 475–486. https://doi.org/10.1016/0040-1951(70)90059-4

Caine, J. S., Evans, J. P., & Forster, C. B. (1996). Fault zone architecture and permeability structure. *Geology*, *24*(11), 1025–1028. https://doi.org/10.1130/0091-7613(1996)0242.3.CO

Cappa, F., Rutqvist, J., & Yamamoto, K. (2009). Modeling crustal deformation and rupture processes related to upwelling of deep CO_2-rich fluids during the 1965–1967 Matsushiro earthquake swarm in Japan. *Journal of Geophysical Research*, *114*(B10304). https://doi.org/10.1029/2009jb006398

Chiaramonte, L., Zoback, M. D., Friedmann, J., & Stamp, V. (2008). Seal integrity and feasibility of CO_2 sequestration in the teapot dome EOR pilot: Geomechanical site characterization. *Environmental Geology*, *54*(8), 1667–1675. https://doi.org/10.1007/s00254-007-0948-7

Chiodini, G., Cardellini, C., Di Luccio, F., Selva, J., Frondini, F., Caliro, S., et al. (2020). Correlation between tectonic CO_2 Earth degassing and seismicity is revealed by a 10-year record in the Apennines, Italy. *Science Advances*, *6*(35), eabc2938. https://doi.org/10.1126/sciadv.abc2938

Cueto-Felgueroso, L., Vila, C., Santillán, D., & Mosquera, J. C. (2018). Numerical modeling of injection-induced earthquakes using laboratory-derived friction laws. *Water Resources Research*, *54*(12), 9833–9859. https://doi.org/10.1029/2017wr022363

Darcy, H. (1856). *Les fontaines publiques de la ville de Dijon Rep*. Dalmont.

Das, I., & Zoback, M. D. (2011). Long-period, long-duration seismic events during hydraulic fracture stimulation of a shale gas reservoir. *Society of Exploration Geophysicists*, *30*(7), 778–786. https://doi.org/10.1190/1.3609093

Den Hartog, S. A. M., & Spiers, C. J. (2014). A microphysical model for fault gouge friction applied to subduction megathrusts. *Journal of Geophysical Research: Solid Earth*, *119*(2), 1510–1529. https://doi.org/10.1002/2013JB010580

Detournay, E., & Cheng, H. D. (1993). Fundamentals of poroelasticity. *Anal Des Methods*, *140*(1), 113–171. https://doi.org/10.1016/B978-0-08-040615-2.50011-3

Dieterich, J. H. (1972). Time-dependent friction in rocks. *Journal of Geophysical Research*, *77*(20), 3690–3697. https://doi.org/10.1029/JB077i020p03690

Fan, Z. Q., Eichhubl, P., & Newell, P. (2019). Basement fault reactivation by fluid injection into sedimentary reservoirs: Poroelastic effects. *Journal of Geophysical Research: Solid Earth*, *124*(7), 7354–7369. https://doi.org/10.1029/2018jb017062

Farrell, N. J. C., Healy, D., & Taylor, C. W. (2014). Anisotropy of permeability in faulted porous sandstones. *Journal of Structural Geology*, *63*(3), 50–67. https://doi.org/10.1016/j.jsg.2014.02.008

Foulger, G. R., Wilson, M. P., Gluyas, J. G., Julian, B. R., & Davies, R. J. (2018). Global review ofhuman-induced earthquakes. *Earth-Science Reviews*, *178*, 438–514. https://doi.org/10.1016/j.earscirev.2017.07.008

French, M. E., Zhu, W., & Banker, J. (2016). Fault slip controlled by stress path and fluid pressurization rate. *Geophysical Research Letters*, *43*(9), 4330–4339. https://doi.org/10.1002/2016gl068893

Gan, Q., & Lei, Q. (2020). Induced fault reactivation by thermal perturbation in enhanced geothermal systems. *Geothermics*, *86*, 101814. https://doi.org/10.1016/j.geothermics

Goodfellow, S. D., Nasseri, M. H. B., Maxwell, S. C., & Young, R. P. (2015). Hydraulic fracture energy budget: Insights from the laboratory. *Geophysical Research Letters*, *42*(9), 3179–3187. https://doi.org/10.1002/2015GL063093

Gu, J. C., Rice, J. R., Ruina, A. L., & Tse, S. T. (1984). Slip motion and stability of a single degree of freedom elastic system with rate and state dependent friction. *Journal of the Mechanics and Physics of Solids*, *32*(3), 167–196. https://doi.org/10.1016/0022-5096(84)90007-3

Guglielmi, Y., Cappa, F., Avouac, J.-P., Henry, P., & Elsworth, D. (2015). Seismicity triggered by fluid injection–induced aseismic slip. *Science*, *348*(6240), 1224–1226. https://doi.org/10.1126/science.aab0476

Healy, J. H., Rubey, W. W., Griggs, D. T., & Raleigh, C. B. (1968). The Denver earthquakes. *Science*, *161*(3848), 1301–1310. https://doi.org/10.1126/science.161.3848.1301

Improta, L., Valoroso, L., Piccinini, D., & Chiarabba, C. (2015). A detailed analysis of wastewater-induced seismicity in the Val d'Agri oil field (Italy). *Geophysical Research Letters*, *42*(8), 2682–2690. https://doi.org/10.1002/2015gl063369

Ito, Y., & Ikari, M. J. (2016). Velocity- and slip-dependent weakening in simulated fault gouge: Implications for multimode fault slip. *Geophysical Research Letters*, *42*(21), 9247–9254. https://doi.org/10.1002/2015GL065829

Iverson, R. M. (2005). Regulation of landslide motion by dilatancy and pore pressure feedback. *Journal of Geophysical Research*, *110*(F2), F02015. https://doi.org/10.1029/2004jf000268

Jaeger, J. C., Cook, N. G., & Zimmerman, R. (2009). *Fundamentals of rock mechanics*. John Wiley and Sons.

James, H. D. (1978). Time-dependent friction and the mechanics of stick-slip. *Pure and Applied Geophysics*, *116*(4–5), 790–806. https://doi.org/10.1007/BF00876539

James, P. V. (2014). Significance for secure CO_2 storage of earthquakes induced by fluid injection. *Environmental Research Letters*, *9*(6), 064022. https://doi.org/10.1088/1748-9326/9/6/064022

Kang, J. Q., Zhu, J. B., & Zhao, J. (2019). A review of mechanisms of induced earthquakes: From a view of rock mechanics. *Geomechanics and Geophysics for Geo-Energy and Geo-Resources*, *5*(2), 171–196. https://doi.org/10.1007/s40948-018-00102-z

Keranen, K. M., Weingarten, M., Abers, G. A., Bekins, B. A., & Ge, S. (2014). Induced earthquakes. Sharp increase in central Oklahoma seismicity since 2008 induced by massive wastewater injection. *Science*, *345*(6195), 448–451. https://doi.org/10.1126/science.1255802

Kim, W. Y. (2013). Induced seismicity associated with fluid injection into a deep well in Youngstown, Ohio. *Journal of Geophysical Research: Solid Earth*, *118*(7), 3506–3518. https://doi.org/10.1002/jgrb.50247

Knipe, R. J. (1992). Faulting processes and fault seal. *Structural & Tectonic Modelling & Its Application to Petroleum Geology*, *1*, 325–342. https://doi.org/10.1016/B978-0-444-88607-1.50027-9

Kwiatek, G., Saarno, T., Bluemle, T., Bonhoff, M., Chendorain, M., Dresen, G., et al. (2019). Controlling fluid-induced seismicity during a 6.1-km-deep geothermal stimulation in Finland. *Science Advances*, *5*, eaav7224. https://doi.org/10.1126/sciadv.aav7224

Langenbruch, C., & Zoback, M. D. (2016). How will induced seismicity in Oklahoma respond to decreased saltwater injection rates? *Science Advances*, *2*(11), 9. https://doi.org/10.1126/sciadv.1601542

Leeman, J. R., Saffer, D. M., Scuderi, M. M., & Marone, C. (2016). Laboratory observations of slow earthquakes and the spectrum of tectonic fault slip modes. *Nature Communications*, *7*(1), 11104. https://doi.org/10.1038/ncomms11104

Li, B. Y., Akhmedov, N. G., Hopkinson, D., Hoffman, J., Duan, Y., Egbebi, A., et al. (2016). Phase change amino acid salt separates into CO_2-rich and CO_2-lean phases upon interacting with CO_2. *Applied Energy*, *161*, 41–47. https://doi.org/10.1016/j.apenergy.2015.09.094

Li, Z., Elsworth, D., Wang, C., Boyd, L., Frone, Z., Metcalfe, E., et al. (2021). Constraining maximum event magnitude during injection-triggered seismicity. *Nature Communications*, *12*(1), 1528–1536. https://doi.org/10.1038/s41467-020-20700-4

Linker, M. F., & Dieterich, J. H. (1992). Effects of variable normal stress on rock friction: Observations and constitutive equations. *Journal of Geophysical Research*, *97*(B4), 4923–4940. https://doi.org/10.1016/0148-9062(93)90292-L

Liu, J., Chen, Z., Elsworth, D., Miao, X., & Mao, X. (2010). Evaluation of stress-controlled coal swelling processes. *International Journal of Coal Geology*, *83*(4), 446–455. https://doi.org/10.1016/j.coal.2010.06.005

Liu, Z., Cheng, Y., Wang, L., Wang, H., Jiang, J., & Li, W. (2018). Analysis of coal permeability rebound and recovery during methane extraction: Implications for carbon dioxide storage capability assessment. *Fuel*, *230*, 298–307. https://doi.org/10.1016/j.fuel.2018.05.057

Luccio, D. F., Chiodini, G., Caliro, S., Cardellini, C., Convertito, V., Pino, N. A., et al. (2018). Seismic signature of active intrusions in mountain chains. *Science Advances*, *4*(1), e1701825. https://doi.org/10.1126/sciadv.1701825

Lucier, A., Zoback, M., Gupta, N., & Ramakrishnan, T. S. (2006). Geomechanical aspects of CO_2 sequestration in a deep saline reservoir in the Ohio River Valley region. *Environmental Geosciences*, *13*(2), 85–103. https://doi.org/10.1306/eg.11230505010

Marone, C. (1998). Laboratory-derived friction laws and their application to seismic faulting. *Annual Review of Earth and Planetary Sciences*, *26*(1), 643–696. https://doi.org/10.1146/annurev.earth.26.1.643

Niemeijer, A., & Spiers, C. J. (2007). A microphysical model for strong velocity weakening in phyllosilicate-bearing fault gouges. *Journal of Geophysical Research*, *112*(B10). https://doi.org/10.1029/2007JB005008

Pacala, S., & Socolow, R. (2004). Stabilization wedges: Solving the climate problem for the next 50 years with current technologies. *Science*, *305*(5686), 968–972. https://doi.org/10.1126/science.1100103

Pampillón, P., Santillan, D., Mosquera, J. C., & Cueto-Felgueroso, L. (2018). Dynamic and quasi-dynamic modeling of injection-induced earthquakes in poroelastic media. *Journal of Geophysical Research: Solid Earth*, *123*(7), 5730–5759. https://doi.org/10.1029/2018jb015533

Rice, J. R. (1993). Spatio-temporal complexity of slip on a fault. *Journal of Geophysical Research*, *98*(B6), 9885–9907. https://doi.org/10.1029/93jb00191

Rice, J. R. (2006). Heating and weakening of faults during earthquake slip. *Journal of Geophysical Research*, *111*(B5), B05311. https://doi.org/10.1029/2005jb004006

Rice, J. R., & Ruina, A. L. (1983). Stability of steady frictional slipping. *Journal of Applied Mechanics*, *50*(2), 343–349. https://doi.org/10.1115/1.3167042

Rice, J. R., & Tse, S. T. (1986). Dynamic motion of a single degree of freedom system following a rate and state dependent friction law. *John Wiley & Sons, Ltd*, *91*(B1), 521–530. https://doi.org/10.1029/JB091iB01p00521

Ruina, A. (1983). Slip instability and state variable friction laws. *Journal of Geophysical Research*, *88*(B12), 10359–10370. https://doi.org/10.1029/JB088iB12p10359

Scuderi, M. M., & Collettini, C. (2016). The role of fluid pressure in induced vs. triggered seismicity: Insights from rock deformation experiments on carbonates. *Scientific Reports*, *6*(1), 24852. https://doi.org/10.1038/srep24852

Segall, P., & Lu, S. (2015). Injection-induced seismicity: Poroelastic and earthquake nucleation effects. *Journal of Geophysical Research: Solid Earth*, *120*(7), 5082–5103. https://doi.org/10.1002/2015jb012060

Segall, P., & Rice, J. R. (1995). Dilatancy, compaction, and slip instability of a fluid-infiltrated fault. *Journal of Geophysical Research*, *1002*(B11), 22155–22172. https://doi.org/10.1029/95JB02403

Segel, L. A., & Slemrod, M. (1989). The quasi-steady-state assumption: A case study in perturbation. *SIAM Review*, *31*(3), 446–477. https://doi.org/10.1137/1031091

Sliaupa, S., Lojka, R., Tasaryova, Z., Kolejka, V., Hladik, V., Kotulova, J., et al. (2013). CO_2 storage potential of sedimentary basins of Slovakia, the Czech Republic, Poland and the Baltic States. *Geological Quarterly*, *57*(2), 219–232. https://doi.org/10.7306/gq.1088

Spagnuolo, E., Nielsen, S., Violay, M., & Di Toro, G. (2016). An empirically based steady state friction law and implications for fault stability. *Geophysical Research Letters*, *43* (7), 3263–3271. https://doi.org/10.1002/2016GL067881

Tang, L. L., Lu, Z., Zhang, M., Sun, L., & Wen, L. X. (2018). Seismicity induced by simultaneous abrupt changes of injection rate and well pressure in Hutubi gas field. *Journal of Geophysical Research: Solid Earth*, *123*(7), 5929–5944. https://doi.org/10.1029/2018jb015863

Terzaghi, K. v. (1923). Die berechnung der durchlassigkeitsziffer des tones aus dem verlauf der hydrodynamischen spannungserscheinungen. Sitzungsberichte der Akademie der Wissenschaften in Wien, Mathematisch-Naturwissenschaftliche Klasse. *Abteilung IIa*, *132*(3–4), 125–138.

Tullis, T. E., & Weeks, J. D. (1986). Constitutive behavior and stability of frictional sliding of granite. *Pure and Applied Geophysics*, *124*(3), 383–414. https://doi.org/10.1007/BF00877209

Verdon, J. P. (2014). Significance for secure CO_2 storage of earthquakes induced by fluid injection. *Environmental Research Letters*, *9*(6), 064022. https://doi.org/10.1088/1748-9326/9/6/064022

Vidal-Gilbert, S., Tenthorey, E., Dewhurst, D., Ennis-King, J., Van Ruth, P., & Hillis, R. (2010). Geomechanical analysis of the Naylor Field, Otway Basin, Australia: Implications for CO_2 injection and storage. *International Journal of Greenhouse Gas Control*, *4*(5), 827–839. https://doi.org/10.1016/j.ijggc.2010.06.001

Vivek, R., & Kumar, G. S. (2019). An improved brine-relative permeability model with hysteresis and its significance to sequestrated CO_2 in a deep saline aquifer. *Environmental Earth Sciences*, *78*(5), 1–15. https://doi.org/10.1007/s12665-019-8174-7

Vrolijk, P. J., Urai, J. L., & Kettermann, M. (2016). Clay smear: Review of mechanisms and applications. *Journal of Structural Geology*, *86*, 95–152. https://doi.org/10.1016/j.jsg.2015.09.006

Wang, L., Kwiatek, G., Rybacki, E., Bonnelye, A., Bohnhoff, M., & Dresen, G. (2020). Laboratory study on fluid-induced fault slip behavior: The role of fluid pressurization rate. *Geophysical Research Letters*, *47*(6). https://doi.org/10.1029/2019GL086627

Warpinski, N. R. R., Du, J., & Zimmer, U. (2012). Measurements of hydraulic-fracture-induced seismicity in gas shales. *SPE Production and Operations*, *27*(03), 240–252. https://doi.org/10.2118/151597-pa

Weingarten, M., Ge, S., Godt, J. W., Bekins, B. A., & Rubinstein, J. L. (2015). High-rate injection is associated with the increase in US mid-continent seismicity. *Science*, *348*(6241), 1336–1340. https://doi.org/10.1126/science.aab1345

Ye, Z., & Ghassemi, A. (2018). Injection-induced shear slip and permeability enhancement in granite fractures. *Journal of Geophysical Research: Solid Earth*, *123*(10), 9009–9032. https://doi.org/10.1029/2018jb016045

Yehya, A., Basbous, J., & Maalouf, E. (2022). Analysis of the hydrogeological conditions affecting fault response to nearby hydraulic fracturing. *Journal of Geophysical Research: Solid Earth*, *127*(10). https://doi.org/10.1029/2022jb024881

Yehya, A., Yang, Z., & Rice, J. R. (2018). Effect of fault architecture and permeability evolution on response to fluid injection. *Journal of Geophysical Research: Solid Earth*, *123*(11), 9982–9997. https://doi.org/10.1029/2018JB016550

Zhu, J. B., & Kang, J. Q. (2020). Fluid injection-induced seismicity considering secondary damage and heterogeneity in the surrounding rock. *Bulletin of Engineering Geology and the Environment*, *79*(5), 2635–2646. https://doi.org/10.1007/s10064-019-01676-y

Zoback, M. D., & Gorelick, S. M. (2012). Earthquake triggering and large-scale geologic storage of carbon dioxide. *Proceedings of the National Academy of Sciences of the United States of America*, *109*(26), 10164–10168. https://doi.org/10.1073/pnas.1202473109